

---

# Application of Genetic Algorithms to *In Situ* Particle Sizing

Michael R. McKee

OL-AC Phillips Laboratory/RKS  
10 East Saturn Blvd.  
Edwards AFB CA 93524-7680

July 1997

Final Report

---

APPROVED FOR PUBLIC RELEASE; DISTRIBUTION UNLIMITED.

---

19970814 088



**PHILLIPS LABORATORY**  
**Propulsion Directorate**  
**AIR FORCE MATERIEL COMMAND**  
**EDWARDS AIR FORCE BASE CA 93524-7048**


## NOTICE

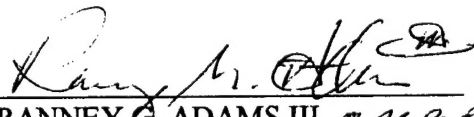
When U.S. Government drawings, specifications, or other data are used for any purpose other than a definitely related Government procurement operation, the fact that the Government may have formulated, furnished, or in any way supplied the said drawings, specifications, or other data, is not to be regarded by implication or otherwise, or in any way licensing the holder or any other person or corporation, or conveying any rights or permission to manufacture, use or sell any patented invention that may be related thereto.

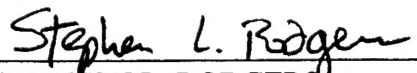
## FOREWORD

This final technical report, entitled "Application of Genetic Algorithms to *In Situ* Particle Sizing," presents the results of an in-house study performed under JON OSATKAAC by OL-AC PL/RKS, Edwards AFB CA. The Principal Investigator/Project Manager for Phillips Laboratory was Michael R. McKee.

This report has been reviewed and is approved for release and distribution in accordance with the distribution statement on the cover and on the SF Form 298.

  
MICHAEL R. McKEE  
Project Manager

  
RANNEY G. ADAMS III *ALP 97-013*  
Public Affairs Director

  
STEPHEN L. RODGERS  
Director  
Propulsion Sciences Division

<b>REPORT DOCUMENTATION PAGE</b>			<b>Form Approved</b> <b>OMB No 0704-0188</b>	
Public reporting burden for this collection of information is estimated to average 1 hour per response, including the time for reviewing instructions searching existing data sources gathering and maintaining the data needed, and completing and reviewing the collection of information. Send comments regarding this burden estimate or any other aspect of this collection of information, including suggestions for reducing this burden to Washington Headquarters Services, Directorate for Information Operations and Reports, 1215 Jefferson Davis Highway, Suite 1204, Arlington, VA 22202-4302, and to the Office of Management and Budget, Paperwork Reduction Project (0740-0188), Washington DC 20503.				
1. AGENCY USE ONLY (LEAVE BLANK)		2. REPORT DATE July 1997		3. REPORT TYPE AND DATES COVERED Final
4. TITLE AND SUBTITLE <b>Application of Genetic Algorithms to <i>In Situ</i> Particle Sizing</b>			5. FUNDING NUMBERS C: PE: PR: OSAT TA: KAAC	
6. AUTHOR(S) <b>Michael R. McKee</b>				
7. PERFORMING ORGANIZATION NAME(S) AND ADDRESS(ES) Phillips Laboratory OL-AC PL/RKS 10 East Saturn Blvd. Edwards AFB CA 93524-7680			8. PERFORMING ORGANIZATION REPORT NUMBER  PL-TR-96-3027	
9. SPONSORING/MONITORING AGENCY NAME(S) AND ADDRESS(ES)			10. SPONSORING/MONITORING AGENCY REPORT NUMBER	
11. SUPPLEMENTARY NOTES:  COSATI CODE(S): 210802; 210902; 0602				
12a. DISTRIBUTION/AVAILABILITY STATEMENT  Approved for Public Release. Distribution Unlimited.			12b. DISTRIBUTION CODE  A	
13. ABSTRACT (MAXIMUM 200 WORDS) Particulates in the solid rocket exhaust plume cause rocket base heating, motor performance losses, and determine the plume spectral properties. The particle properties that contribute to these effects are the particle size distribution function (PSDF), emissivity, density, and surface tension. Of the four, the PSDF and emissivity are not very well known. Until an adequate model is developed for the PSDF and emissivity, <i>in situ</i> measurements will have to be made. This report reviews the motivation behind the design and development of an <i>in situ</i> optical probe, and discusses the development of the theory needed to make the measurements of the optical properties. It also develops an estimate of the sampling time required to make the measurements statistically meaningful. Consideration is given to the effects that the optical properties play in the scattering of light by the particles and scanning angles, and incident polarizations were chosen that would minimize these effects. PSDF is discussed, with recognition given to the degree of difficulty in applying analytic methods. Various optimization methods are discussed, especially Genetic Algorithms (GA). The report closes on the note that the PSDF was discernible by transforming it into the equivalent integrated mass distribution (IMD), and recommendations are given as to further improvements in the GA approach.				
14. SUBJECT TERMS genetic algorithm; optical probe; in situ optical probe; liquid semiconductors; aluminum oxide; rocket motor; remote sensing; emissivity; Fredholm integrals; ill-conditioned matrices			15. NUMBER OF PAGES 50	
			16. PRICE CODE	
17. SECURITY CLASSIFICATION OF REPORT <b>Unclassified</b>	18. SECURITY CLASSIFICATION OF THIS PAGE <b>Unclassified</b>	19. SECURITY CLASSIFICATION OF ABSTRACT <b>Unclassified</b>	20. LIMITATION OF ABSTRACT <b>SAR</b>	

## TABLE OF CONTENTS

Section	Page
1.0 INTRODUCTION	1
2.0 ORIGIN OF THE OPTICAL PROPERTIES FOR ELASTIC SCATTERING	3
3.0 THE SCATTERING OF LIGHT WAVES BY SPHERICAL PARTICLES	5
4.0 MEASURING THE OPTICAL PARAMETERS	11
5.0 INSTRUMENT DESIGN	13
6.0 TENTATIVE OPTICAL INSTRUMENT DESIGN	15
7.0 FIRST ORDER DETERMINATION OF THE PARTICLE SIZE DISTRIBUTION FUNCTION (PSDF)	17
8.0 CONCLUSIONS	38
9.0 REFERENCES	40

## LIST OF FIGURES

Figure		Page
1	Scattering of a Plane Wave by a Spherical Particle	6
2	The Four-Modulator Photopolarimeter	11
3	The Relation Between the Incident Source Position Vector and the Scattered Detector Vector	13
4	The <i>In Situ</i> Particle Probe, Based upon the Presented Theoretical Discussions	16
5	Singular Values of a 64 by 100 Scattering Matrix	18
6	Intensity versus Angle Scattering for Perpendicular Polarization, $ S_1 ^2$	20
7	Intensity versus Angle Scattering for Parallel Polarization, $ S_2 ^2$	22
8	Trial Solutions $\hat{a}$ and $\hat{b}$ Converging to $\hat{c}$	23
9	Cumulative Sum and Random Selection	24
10	Larger Values are Selected More Often	25
11	One-Point Crossover	26
12	Two-Point Crossover	26
13	Bit Masked Crossover	27
14	First Results Using CGA	29
15	Outline of Adaptive Procedure	30
16	Comparison of Modified Boltzman to Standard Boltzman Used in Simulated Annealing	32
17	Comparison of Non-scaled and Scaled Selection Results	32
18	Bimodal Integrated Mass Distribution	33
19	Integrated Mass Distribution with Piecewise Fit Overlaid	34
20	Preliminary Results Derived with SAGA	35
21	Comparison of SAGA Derived with Unknown Intensities	36
22	Improved Results After Modifications with SAGA	36
23	Before-and-After Results	37

## GLOSSARY

AGA	adaptive genetic algorithm
Al <sub>2</sub> O <sub>3</sub>	aluminum oxide
ASM	amplitude scattering matrix
csp	cumulative sum probability
EMF	electromagnetic field
EMW	electromagnetic waves
CGA	combinatorial genetic algorithm
CN	condition number
GA	genetic algorithm
GMD	Gaussian monomodal distribution
IMD	integrated mass distribution
IR	infrared
MSE	mean-squared error
PSA	polarization state analyzer
PSDF	particle size distribution function
PSD	polarization state detector
PSG	polarization state generator
PVDF	particle volume density function
qcsp	complement of cumulative sum probability
SAGA	simulated annealing genetic algorithm
T	temperature(s)

## 1.0 INTRODUCTION

Particulates in the solid rocket exhaust plume cause rocket base heating, motor performance losses, and determine the plume spectral properties (Refs. 1 to 21). The particle properties that contribute to these effects are the particle size distribution function (PSDF), emissivity,  $\epsilon_\lambda$ , density, and surface tension. Of the four, the PSDF and  $\epsilon_\lambda$  are not very well known. Exhaust plume modeling is used to predict the degree of base heating, performance losses, and the plume spectral properties. PSDF is determined by collisions, shear, and acceleration of the particles in the throat region of the nozzle.  $\epsilon_\lambda$  is a function of intrinsic and extrinsic material properties and the PSDF. Until an adequate model is developed for the PSDF and  $\epsilon_\lambda$ , *in situ* measurements will have to be made.

For the conventional aluminized solid propellant rocket motor, the chief particulate material is aluminum oxide,  $\text{Al}_2\text{O}_3$ . It occurs in the liquid phase and the solid alpha and gamma phases. While  $\text{Al}_2\text{O}_3$  is an insulator in the solid phase, emissivity is very small. Liquid phase  $\text{Al}_2\text{O}_3$  becomes a class  $\text{A}_2^{\text{III}} \text{B}_3^{\text{VI}}$  semiconductor with free carrier processes dominant. This causes  $\text{Al}_2\text{O}_3$  to be a source of extremely intense continuum emission.

The solid state physics community believes that a liquid semiconductor can be modeled using solid amorphous semiconductor theory. The momentum selection rules for optical transitions are relaxed, all infrared and Raman modes contribute to the absorption spectra, and the optical absorption edge becomes featureless. Allowed bands and energy gaps still occur because the form of the density of states versus the energy is determined most strongly by electron bonding configurations, which are modified by the presence of dangling bonds and defects. These effects may consist of pinning the Fermi energy and will vary strongly with temperature. This will have a significant effect on the conductivity,  $\sigma$ , and the dielectric constant,  $\epsilon$ , which determine the behavior of the media's optical properties. There has been much work in determining the material properties of  $\text{Al}_2\text{O}_3$ . (To get a much deeper sense of the results, read Ref. 6.)

Suppose that both the PSDF and the  $\epsilon_\lambda$  are known for a range of wavelengths,  $\lambda$ , and temperatures,  $T$ , and that the particles are a Lambertian source, the power  $\Phi_{\text{det}}$  (radiant flux) seen at a detector whose distance from the particles is much greater than the particle diameters,  $D$ , with the field of view,  $\Omega_{\text{det}}$ , would be

$$\Phi_{\text{det}} = Le \times \Omega_{\text{det}} \times \int_0^\infty n(D, \mathfrak{r}) \cdot \frac{\pi}{4} D^2 dD \quad (1)$$

where  $n(D, \mathfrak{r})$  is the PSDF at the spacial position  $\mathfrak{r}$ . The Lambertian radiance,  $Le$ , for the particle is defined as

$$Le = \frac{\int_{\lambda_1}^{\lambda_2} M_e(\lambda, T) d\lambda}{\pi} \times \frac{\pi}{4} D^2 \quad (2)$$

where the excittance,  $M_e$  is

$$M_e(\lambda, T) = \varepsilon_\lambda \left( \frac{2\pi h_B c^2 \lambda^{-5}}{\exp(hc/(k_B \lambda T)) - 1} \right) \quad (3)$$

These formulas show how the material properties and the PSDF contribute to  $\varepsilon_\lambda$ .

The imaginary part,  $k$ , of the refractive index  $m$ , controls the visible to mid-IR emission of micron sized particles. For small values of the spectral emissivity,  $\varepsilon_\lambda$ , the emissivity of  $\text{Al}_2\text{O}_3$  is nearly linear with respect to the imaginary refractive index,  $k$ . The approximate relation is

$$\varepsilon_\lambda \approx 2k \left( \frac{D}{\lambda} \right). \quad (4)$$

There are various formulations for  $k$ . The following formula, a combination of physical models and curve fits from a Russian paper (Ref. 10), is

$$k = \chi_0 + \chi_1 + \chi_2 + \chi_3. \quad (5)$$

The vibration band properties are given by  $\chi_0$ , which is defined as

$$\chi_0 = 7.93 \times 10^{-4} \lambda \cdot \exp\left(-\frac{6.07 \times 10^{-3}}{T} \left(\frac{10^4}{\lambda} - 1333\right)^2\right) \left(1 - \exp\left(-\frac{1.917 \times 10^3}{T}\right)\right). \quad (6)$$

The free-free electron transition model is

$$\chi_1 = 1.0 \times 10^{-2} \cdot \frac{\lambda}{z} \cdot \exp\left(-\frac{7.2 \times 10^3}{T \lambda_g}\right). \quad (7)$$

The fundamental edge band model is

$$\chi_2 = 2.1 \times 10^{-9} \cdot \lambda \left( \frac{1}{\lambda} - \frac{2}{\lambda_g} \right) T^2 + 1.5 \times 10^{-2} (\lambda_g/2) \quad \lambda \geq \lambda_g \quad (8)$$

The Urbach edge, which contributes to the UV absorption characteristics, is

$$\chi_3 = 1.5 \times 10^{-2} \lambda \exp\left(-\frac{2.8 \times 10^3}{T} \left(\frac{2}{\lambda_g} - \frac{1}{\lambda}\right)\right) \quad \lambda < \lambda_g/2 \quad (9)$$

where  $z$  is given as

$$z = \left\{ 1 + \lambda^2 \left( \frac{1.02378}{\lambda^2 - 0.00377588} + \frac{1.058264}{\lambda^2 - 0.0122544} + \frac{5.280792}{\lambda^2 - 321.36164} \right) \right\}^{0.5} \times \left[ 1 + 0.029 \left( \frac{T}{1000} - 0.473 \right) \right] \quad (10)$$

and  $\lambda_g$  is given as



$$\frac{1}{\lambda_g} = 0.6916 \left( \frac{1.289 \times 10^4}{T} - 3.233 \right) \quad (11)$$

This formula was presented by the Russians at the AIAA 28th Thermophysics Conference (Ref. 10). While it seems to include all the relevant models, there is some debate as to its accuracy. In the solid phases,  $\text{Al}_2\text{O}_3$  has the property of birefringence. This has the effect of inducing ellipticity into an incident plane electromagnetic wave. In a cloud of randomly oriented scatters, its effect should be negligible. However, the plume flow field will induce some coherent orientation of the particulates. Optical activity may play a role in plume spectral scattering.

With this in mind, this report describes the design considerations for an *in situ* optical probe to measure optical properties and the PSDF of  $\text{Al}_2\text{O}_3$  or any other particles in an exhaust plume.

## 2.0 ORIGIN OF THE OPTICAL PROPERTIES FOR ELASTIC SCATTERING

The two parameters that determine the optical properties for a non-magnetic material (the permittivity,  $\mu = 1$ ) are the dielectric constant,  $\epsilon$ , which defines the magnitude of the displacement currents due to the time variation of the external field,  $\vec{E}$ , and the conductivity,  $\sigma$ , which is a measure of the real currents created in the media by the external field,  $\vec{E}$  (Refs. 22 to 30). Given the solutions for the incident time varying electric field,

$$\vec{E}_i = E_0 \exp(j(\omega t - kz)) \quad (12)$$

and its associated magnetic field intensity,

$$\vec{H} = \frac{k}{\omega \mu} E_0 \exp(j(\omega t - kz)) \quad (13)$$

we can derive from the solutions of Maxwell's equations, for an attenuated wave in a conducting media;

Given

$$\begin{aligned} \nabla^2 \vec{E} - \epsilon \mu \frac{\partial^2 \vec{E}}{\partial t^2} - \sigma \mu \frac{\partial \vec{E}}{\partial t} &= \nabla \frac{\rho_f}{\epsilon} = 0 \\ \nabla^2 \vec{H} - \epsilon \mu \frac{\partial^2 \vec{H}}{\partial t^2} - \sigma \mu \frac{\partial \vec{H}}{\partial t} &= 0 \end{aligned} \quad (14)$$

we can derive the complex wavenumber,

$$K^2 = 2\pi \frac{\epsilon\mu}{\lambda_0^2} \left(1 - \frac{j\sigma}{\omega\epsilon}\right) \quad (15)$$

The real and imaginary components of the complex wavenumber,  $K = k_r + jk_i$ , are;

$$\begin{aligned} k_r &= \frac{2\pi}{\lambda} \left(\frac{\epsilon_r\mu_r}{2}\right)^{1/2} \left\{ \left(1 + \left(\frac{\sigma}{\omega\epsilon}\right)^2\right)^{1/2} + 1 \right\}^{1/2} \\ k_i &= \frac{2\pi}{\lambda} \left(\frac{\epsilon_r\mu_r}{2}\right)^{1/2} \left\{ \left(1 + \left(\frac{\sigma}{\omega\epsilon}\right)^2\right)^{1/2} - 1 \right\}^{1/2} \end{aligned} \quad (16)$$

where  $\epsilon_r$  and  $\mu_r$  are the relative dielectric and permittivity constants. We can convert the complex wavenumber,  $K$ , into the complex refractive index,  $\tilde{m}$ , by

$$\begin{aligned} k_r + jk_i &= (n^2 - k^2) + i2nk \\ n &= \sqrt{\frac{|k_r + jk_i| - k_r}{2}} \\ k &= \sqrt{\frac{|k_r + jk_i| + k_r}{2}} \\ \tilde{m} &= n + jk \end{aligned} \quad (17)$$

where  $n$  is a function of the media's phase velocity and  $k$  is the attenuation factor of the electromagnetic waves traveling through the media. Thus, if the wavelength and temperature dependent functions for the dielectric constant and the conductivity are known, the complex refractive index can be easily calculated.

Using ellipsometric techniques, degree of polarization and phase delay that the media has on an incident plane wave can be measured. From these measurements the complex wavenumber,  $k$ , can be deduced. The amount of ellipsicity induced by the material is measured by the use of polarizers and retarders. The resulting ellipsometric measurements are represented by the Stoke's vector,  $\hat{S}$ , where  $\hat{S}$  is composed of;

$$\hat{S} = \begin{bmatrix} I \\ Q \\ U \\ V \end{bmatrix} = \begin{bmatrix} \text{Total\_Intensity} \\ I \cdot p \cdot \cos(2\eta) \cdot \cos(2\gamma) \\ I \cdot p \cdot \cos(2\eta) \cdot \sin(2\gamma) \\ I \cdot p \cdot \sin(2\eta) \end{bmatrix} \quad (18)$$

where the degree of polarization,  $p$ , is given by

$$p = \frac{\sqrt{Q^2 + U^2 + V^2}}{I_0} \quad (19)$$

the azimuth,  $\gamma$ , and the ellipticity,  $\eta$ , are related to the Stokes vector elements by

$$\begin{aligned} \gamma &= \frac{1}{2} \text{atan} \frac{V}{Q} & 0 \leq \gamma < \pi \\ \eta &= \frac{1}{2} \text{atan} \frac{V}{\sqrt{Q^2 + U^2}} & -\frac{\pi}{4} \leq \eta \leq \frac{\pi}{4} \end{aligned} \quad (20)$$

the complex wavenumber,  $K$ , is given by

$$\begin{aligned} k_r &= \sin(\varphi)^1 \tan(\varphi)^1 \frac{\cos(2\psi)^1 - \sin(2\psi)^1 \sin(\Delta)^1}{(1 + \cos(\Delta) \sin(2\psi))^1} - \sin(\theta)^2 \\ k_i &= \frac{2 \sin(2\psi) \cos(2\psi) \sin(\Delta)}{(1 + \cos(\Delta) \sin(2\psi))^2} \sin(\theta)^2 \tan(\theta)^2 \end{aligned} \quad (21)$$

the angles,  $\psi$  and  $\Delta$  are related to the Stokes vector elements,  $V$ ,  $Q$ , and  $U$ , by

$$\begin{aligned} \psi &= \frac{1}{2} \text{atan} \frac{\sqrt{V^2 + Q^2}}{-Q} \\ \Delta &= \text{atan} \frac{-V}{U} \end{aligned} \quad (22)$$

and  $\theta$  is the scattering angle.

### 3.0 THE SCATTERING OF LIGHT WAVES BY SPHERICAL PARTICLES

The development of the closed form of the solutions to Maxwell's equations for a spherical particle has been credited to Gustav Mie in 1908. For the theoretical development see References 23 and 24.

Figure 1 shows a single spherical particle, with particle size parameter,  $x = k(D/2)$ , illuminated by a laser of wavelength  $\lambda$ , and a beam width much larger than the diameter of the particle. The polarization of the laser's electromagnetic waves (EMW) is given by the polarization of the electric field component. Figure 1 shows both  $x$  and  $y$  polarizations for two separate electromagnetic waves.

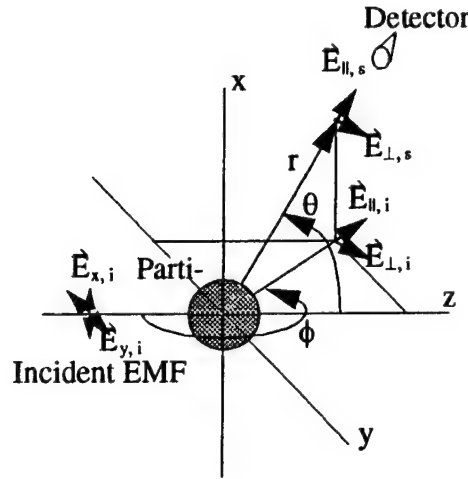


**Figure 1**  
**Scattering of a Plane Wave by a Spherical Particle**

With the wavenumber of the surrounding medium is  $k = 2\pi(N/\lambda)$ , the electric field portion of the solution to Maxwell's equations for the elastically scattered electromagnetic wave in the far field (at the detector) is given by

$$\begin{bmatrix} E_{||,s} \\ E_{\perp,s} \end{bmatrix} = \left( \frac{e^{ik(r-z)}}{-ikr} \right) \begin{bmatrix} s_2(\theta, \tilde{m}, x) & s_3(\theta, \tilde{m}, x) \\ s_4(\theta, \tilde{m}, x) & s_1(\theta, \tilde{m}, x) \end{bmatrix} \begin{bmatrix} \cos \phi & \sin \phi \\ \sin \phi & -\cos \phi \end{bmatrix} \begin{bmatrix} E_{x,i} \\ E_{y,i} \end{bmatrix} \quad (23)$$

The amplitude scattering matrix (ASM),

$$\left( \frac{e^{ik(r-z)}}{-ikr} \right) \begin{bmatrix} s_2(\theta, \tilde{m}, x) & s_3(\theta, \tilde{m}, x) \\ s_4(\theta, \tilde{m}, x) & s_1(\theta, \tilde{m}, x) \end{bmatrix} \quad (24)$$

contains information about the particle shape, size, and the material's optical properties. The elements,  $s_i$ , of the ASM are of the form

$$s_1(\theta, \tilde{m}, x) = \sum_{n=1}^{\infty} \frac{2n+1}{n(n+1)} (a_n \tau_n + b_n \pi_n) \quad (25)$$

$$s_2(\theta, \tilde{m}, x) = \sum_{n=1}^{\infty} \frac{2n+1}{n(n+1)} (a_n \pi_n + b_n \tau_n) \quad (26)$$

$$s_3(\theta, \tilde{m}, x) = \sum_{n=1}^{\infty} \frac{2n+1}{n(n+1)} c_n (\tau_n + \pi_n) \quad (27)$$

$$s_4(\theta, \tilde{m}, x) = -s_3(\theta, \tilde{m}, x) \quad (28)$$

For the case of a particle that consists of an optically active material, the coefficients  $a_n$ ,  $b_n$ , and  $c_n$  are

$$\begin{aligned} a_n &= \frac{V_n(R)A_n(L) + V_n(L)A_n(R)}{W_n(L)V_n(R) + V_n(L)W_n(R)} \\ b_n &= \frac{W_n(L)B_n(R) + W_n(R)B_n(L)}{W_n(L)V_n(R) + V_n(L)W_n(R)} \\ c_n &= \frac{W_n(R)A_n(L) - W_n(L)A_n(R)}{W_n(L)V_n(R) + V_n(L)W_n(R)} \end{aligned} \quad (29)$$

where  $R$  and  $L$  refer to the right- and left-handed circular polarization effects that the material imposes upon the incident electromagnetic field,  $\vec{E}_i$ . The components making up the coefficients  $a_n$ ,  $b_n$ , and  $c_n$  consist of the spherical Bessel functions,  $\psi_n(\rho) = \rho j_n(\rho)$ , and the spherical Hankel functions,  $\xi_n(\rho) = \rho h_n(\rho)$ .  $J$  can be replaced with  $R$  or  $L$ .

$$\begin{aligned} W_n(J) &= \tilde{m} \psi_n(\tilde{m}Jx) \xi'_n(x) - \xi_n(x) \psi'_n(\tilde{m}Jx) \\ V_n(J) &= \psi_n(\tilde{m}Jx) \xi'_n(x) - \tilde{m} \xi_n(x) \psi'_n(\tilde{m}Jx) \\ A_n(J) &= \tilde{m} \psi_n(\tilde{m}Jx) \psi'(x) - \psi_n(x) \psi'_n(\tilde{m}Jx) \\ B_n(J) &= \psi_n(\tilde{m}Jx) \psi'(x) - \tilde{m} \psi_n(x) \psi'_n(\tilde{m}Jx) \end{aligned} \quad (30)$$

The relative refractive indices  $\tilde{m}_L$ ,  $\tilde{m}_R$  and the mean refractive index  $\tilde{m}$  are defined as:

$$\tilde{m}_L = \frac{N_L}{N} \quad \tilde{m}_R = \frac{N_R}{N} \quad \frac{1}{\tilde{m}} = \frac{1}{2} \left( \frac{1}{\tilde{m}_R} + \frac{1}{\tilde{m}_L} \right) \cdot \frac{\mu_1}{\mu} \quad (31)$$

where  $\mu_1$  is permeability of the spherical material and  $\mu$  is the permeability of the surrounding medium. When the material has zero optical activity,  $m_L = m_R$  and the scattering coefficients  $a_n$ ,  $b_n$ , and  $c_n$  reduce to

$$a_n = \left( \frac{A_n}{W_n} \right) = \frac{\tilde{m} \psi_n(\tilde{m}x) \psi'(x) - \psi_n(x) \psi'_n(\tilde{m}x)}{\tilde{m} \psi_n(\tilde{m}x) \xi'_n(x) - \xi_n(x) \psi'_n(\tilde{m}x)} \quad (32)$$

$$b_n = \left( \frac{B_n}{V_n} \right) = \frac{\psi_n(\tilde{m}x) \psi'(x) - \tilde{m} \psi_n(x) \psi'_n(\tilde{m}x)}{\psi_n(\tilde{m}x) \xi'_n(x) - \tilde{m} \xi_n(x) \psi'_n(\tilde{m}x)} \quad (33)$$

$$c_n = 0 \quad (34)$$

This, in turn, would reduce the off diagonal elements of the ASM to zero. The scattered electromagnetic field becomes;

$$\begin{bmatrix} E_{x,s} \\ E_{y,s} \end{bmatrix} = \begin{pmatrix} e^{ik(r-z)} \\ -ikr \end{pmatrix} \begin{bmatrix} S_2(\theta, \tilde{m}, x) & 0 \\ 0 & S_1(\theta, \tilde{m}, x) \end{bmatrix} \begin{bmatrix} \cos\phi & \sin\phi \\ \sin\phi & -\cos\phi \end{bmatrix} \begin{bmatrix} E_{x,i} \\ E_{y,i} \end{bmatrix} \quad (35)$$

However, it should be noted that changes in the polarization of the scattered wave can be caused by the particle shape. It may not be possible to determine both the shape and the optical properties from scattered wave measurements alone. For a complete derivation of the scattering equations for an optically active particle, refer to Reference 23.

Since most of our measuring devices are sensitive only to intensity, we convert Equation (23) into the intensity, which now has the form

$$I_s = (1/(k^2 r^2)) \underline{\sigma}_{bi} I_i \quad (36)$$

where  $\underline{\sigma}_{bi}$  is the 4 x 4 bistatic Mueller matrix consisting of the intensity scattering coefficients  $f_{ij}$ ,

$$\underline{\sigma}_{bi} = \begin{bmatrix} f_{11} & f_{12} & f_{13} & f_{14} \\ f_{21} & f_{22} & f_{23} & f_{24} \\ f_{31} & f_{32} & f_{33} & f_{34} \\ f_{41} & f_{42} & f_{43} & f_{44} \end{bmatrix}. \quad (37)$$

As stated in Section 2 (Origin of the Optical Properties for Elastic Scattering), optical elements such as polarizers and retarders can be used to extract information about the state of the polarization. This is expressed as the Stokes vectors  $I_s$  and  $I_i$ , which represent the scattered and incident intensities. Equations (38) through (40) show how the parameters of the Stokes vector are related to the electromagnetic wave.

Let the time varying electric field,  $\vec{E}_i$ , be elliptically polarized. This field can be expressed as

$$\vec{E} = \vec{E}_0 \exp(i(kz - \omega t)) \quad \vec{E}_0 = E_{\parallel} \hat{e}_{\parallel} + E_{\perp} \hat{e}_{\perp} \quad (38)$$

where the parallel and perpendicular components with electric field amplitudes,  $a_{\parallel}$ ,  $a_{\perp}$  and phases  $\delta_{\parallel}$ ,  $\delta_{\perp}$ , are

$$E_{\parallel} = a_{\parallel} e^{-i\delta_{\parallel}} \quad E_{\perp} = a_{\perp} e^{-i\delta_{\perp}} \quad (39)$$

Thus, the Stokes vector components are related to the parallel and perpendicular  $\vec{E}_i$  field by

$$\begin{aligned} I_1 &= \langle E_{\parallel} E_{\parallel}^* + E_{\perp} E_{\perp}^* \rangle = \langle a_{\parallel}^2 + a_{\perp}^2 \rangle \\ I_2 &= \langle E_{\parallel} E_{\parallel}^* - E_{\perp} E_{\perp}^* \rangle = \langle a_{\parallel}^2 - a_{\perp}^2 \rangle \\ U &= \langle E_{\parallel} E_{\perp}^* + E_{\perp} E_{\parallel}^* \rangle = \langle 2a_{\parallel} a_{\perp} \cos\delta \rangle \\ V &= i \langle E_{\parallel} E_{\perp}^* - E_{\perp} E_{\parallel}^* \rangle = \langle 2a_{\parallel} a_{\perp} \sin\delta \rangle \end{aligned} \quad (40)$$

where  $I_1$  is the intensity of the received beam,  $I_2$  is the difference for the two perpendicular polarizations of the intensity, and  $U$  and  $V$  describe the effects of the relative delay.

Now, in terms of the incident and scattered electromagnetic fields,

$$\begin{aligned} E_{\parallel, s} &= s_1 E_{\parallel, i} + s_4 E_{\perp, i} \\ E_{\perp, s} &= s_3 E_{\parallel, i} + s_2 E_{\perp, i} \end{aligned} \quad (41)$$

the incident and scattered Stokes vectors, are related to the incident and scattered electric fields by

$$\begin{aligned} I_1 &= (s_1 E_{\parallel, i} + s_4 E_{\perp, i})(s_1 E_{\parallel, i} + s_4 E_{\perp, i})^* + (s_3 E_{\parallel, i} + s_2 E_{\perp, i})(s_3 E_{\parallel, i} + s_2 E_{\perp, i})^* \\ I_2 &= (s_1 E_{\parallel, i} + s_4 E_{\perp, i})(s_1 E_{\parallel, i} + s_4 E_{\perp, i})^* - (s_3 E_{\parallel, i} + s_2 E_{\perp, i})(s_3 E_{\parallel, i} + s_2 E_{\perp, i})^* \\ U &= (s_1 E_{\parallel, i} + s_4 E_{\perp, i})(s_3 E_{\parallel, i} + s_2 E_{\perp, i})^* + (s_3 E_{\parallel, i} + s_2 E_{\perp, i})(s_1 E_{\parallel, i} + s_4 E_{\perp, i})^* \\ V &= i((s_1 E_{\parallel, i} + s_4 E_{\perp, i})(s_3 E_{\parallel, i} + s_2 E_{\perp, i})^* - (s_3 E_{\parallel, i} + s_2 E_{\perp, i})(s_1 E_{\parallel, i} + s_4 E_{\perp, i})^*) \end{aligned} \quad (42)$$

and satisfies the inequality

$$I_1^2 \geq I_2^2 + U^2 + V^2 \quad (43)$$

where the equality holds for completely polarized light. Thus, the ASM is replaced by  $\sigma_{bi}$ , where the matrix elements of  $\sigma_{bi}$  are given as combinations of the electric field scattering matrix elements

$$\begin{aligned} f_{11} &= \frac{1}{2}(|s_1|^2 + |s_2|^2 + |s_3|^2 + |s_4|^2) & f_{31} &= \text{Re}(s_2 s_4^* + s_1 s_3^*) \\ f_{12} &= \frac{1}{2}(|s_2|^2 - |s_1|^2 + |s_4|^2 - |s_3|^2) & f_{32} &= \text{Im}(s_2 s_4^* - s_1 s_3^*) \\ f_{13} &= \text{Re}(s_2 s_3^* + s_1 s_4^*) & f_{33} &= \text{Re}(s_1 s_2^* + s_3 s_4^*) \\ f_{14} &= \text{Im}(s_2 s_3^* + s_1 s_4^*) & f_{34} &= \text{Im}(s_2 s_1^* + s_3 s_4^*) \\ f_{21} &= \frac{1}{2}(|s_2|^2 + |s_1|^2 - |s_4|^2 - |s_3|^2) & f_{41} &= \text{Im}(s_2^* s_4 + s_3^* s_1) \\ f_{22} &= \frac{1}{2}(|s_2|^2 + |s_1|^2 - |s_4|^2 - |s_3|^2) & f_{42} &= \text{Im}(s_2^* s_4 - s_3^* s_1) \\ f_{23} &= \text{Re}(s_2 s_3^* - s_1 s_4^*) & f_{43} &= \text{Im}(s_1 s_2^* - s_3 s_4^*) \\ f_{24} &= \text{Im}(s_2 s_3^* - s_1 s_4^*) & f_{44} &= \text{Re}(s_1 s_2^* - s_3 s_4^*) \end{aligned} \quad (44)$$

The off diagonal elements of  $\sigma_{bi}$  contain information about particle shape and optical activity. If the particle is absolutely spherical and the material making up the particle has zero optical activity, then the scattering matrix becomes

$$\sigma_{bi} = \begin{bmatrix} f_{11} & f_{12} & 0 & 0 \\ f_{21} & f_{22} & 0 & 0 \\ 0 & 0 & f_{33} & f_{34} \\ 0 & 0 & f_{43} & f_{44} \end{bmatrix} \quad (45)$$

and matrix elements  $f_{33}$ ,  $f_{34}$ ,  $f_{43}$ ,  $f_{44}$  become

$$\begin{aligned} f_{33} &= \text{Re}((S_1, S_2^*)) & f_{34} &= -\text{Im}((S_1, S_2^*)) \\ f_{43} &= \text{Im}((S_1, S_2^*)) & f_{44} &= \text{Re}((S_1, S_2^*)) \end{aligned} \quad (46)$$

Up to this point, the calculations have been for coherent electromagnetic waves; however, when a plain, polarized wave passes through a cloud of randomly positioned particles, the coherence is degraded. The degree to which coherency is lost depends upon the particle volume density or the particle volume density function (PVDF), which is the ratio of the volume occupied by the particles to the total volume and the particle optical properties.

Given that the incident wave is coherent, what is the coherence state after a plane wave passes through a cloud of particles? For a cloud of randomly distributed particles, the scattered intensity out of the line of sight of the laser beam will be incoherent. Along the line of sight, however, there exist both the coherent and the incoherent fields caused by the presence of the particles. As the particle density increases, the total intensity,  $I_t$ , decreases, as does the coherent intensity,  $I_c$ . However, the incoherent intensity,  $I_i$ , increases and is predicted by the formula

$$I_i = I_0 \exp(-\gamma) \left( \exp \left( \int_0^{R\infty} \int_0^{R\infty} n(D, x) \sigma_s(D) dD dx \right) - 1 \right) \quad (47)$$

whereas the coherent intensity,  $I_c$ , attenuation can be predicted by

$$I_c = \exp \left( - \int_0^{R\infty} \int_0^{R\infty} n(D, x) \sigma_s(D) dD dx \right) \quad (48)$$

where the optical path,  $\gamma$ , is defined as

$$\gamma = \int_0^{R\infty} \int_0^{R\infty} n(D, x) \sigma_t(D) dD dx \quad (49)$$

$\sigma_s$  is the particle cross section and  $\sigma_t$  is the total cross section. Thus, the greater the particle density, the larger the contribution of multiple scatter. From an instrument design perspective, all optical effects must be modeled. It is desirable to keep multiple scattering effects to a minimum, while insuring that enough particles are observed to make a reasonable statistical sample.



## 4.0 MEASURING THE OPTICAL PARAMETERS

Polarization-state-in/polarization-state-out measurements are needed to measure the 16 elements of  $\underline{\sigma}_{bi}$ , for each possible scattering angle,  $\theta_s$  (Refs. 32, 33). In effect, we present a known Stokes vector state to the system and determine the state of the Stokes vector at the system output. The multi-angle ellipsometer is the instrument that can make these measurements. There are five basic steps in an ellipsometric measurement: (1) providing an incident polarization state; (2) allowing an interaction with the measured system; (3) measuring the emerging polarization state; (4) determining the system parameters which describe the alteration of the polarization state; and (5) inferring the state of the system.

The device developed in Reference 27 is capable of measuring all 16 elements. The device consists of two polarizers and four photo-elastic type modulators. A schematic of the device is shown in Figure 2. For a detailed description, see Reference 33.

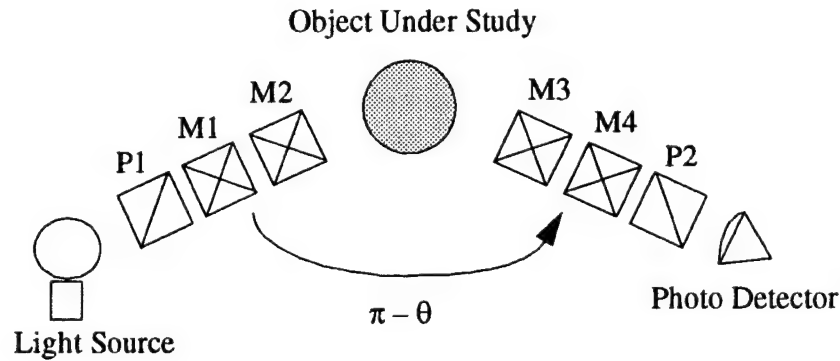


**Figure 2**  
**The Four-Modulator Photopolarimeter**

Light from the laser enters the device through polarizer P1. The modulators, M1 and M2, have their retardance values modulated at frequencies  $\omega_1$  and  $\omega_2$ . The light, with a known elliptical state, is scattered off the sample and into modulators M3 and M4, whose modulation frequencies are  $\omega_3$  and  $\omega_4$ . The scattered, modulated signal passes through the polarizer P2 to the detector. The Stokes-Mueller equation for this is

$$I_r = I_0(P_2 M_4 M_3 \underline{\sigma}_{bi} M_2 M_1 P_1). \quad (50)$$

Performing the matrix multiplications, the signal seen by the detector is given by

$$\begin{aligned}
I_r = \frac{I_0}{2} & (f_{11} + f_{12} \cos \delta_1 + f_{13} \sin \delta_1 \sin \delta_2 - f_{14} \sin \delta_1 \cos \delta_2 + \\
& f_{21} \cos \delta_4 + f_{22} \cos \delta_1 \cos \delta_4 + f_{23} \sin \delta_1 \sin \delta_2 \cos \delta_4 - f_{24} \sin \delta_1 \cos \delta_2 \cos \delta_4 + \\
& f_{31} \sin \delta_3 \sin \delta_4 + f_{32} \cos \delta_1 \sin \delta_3 \sin \delta_4 + f_{33} \sin \delta_1 \sin \delta_2 \sin \delta_3 \sin \delta_4 \\
& - f_{34} \sin \delta_1 \cos \delta_2 \sin \delta_3 \sin \delta_4 + \\
& f_{41} \cos \delta_3 \sin \delta_4 + f_{42} \cos \delta_1 \cos \delta_3 \sin \delta_4 + f_{43} \sin \delta_1 \sin \delta_2 \cos \delta_3 \sin \delta_4 \\
& - f_{44} \sin \delta_1 \cos \delta_2 \cos \delta_3 \sin \delta_4)
\end{aligned} \tag{51}$$

where the modulator retardance values,  $\delta_i$ , are varied sinusoidally at the different frequencies,  $\omega_i$ ,  $i = [1, 4]$ .

$$\delta_i = \delta_{0i} \cos \omega_i t \tag{52}$$

where  $\delta_{0i}$  is the initial phase angle of the retarder.

Because the effective component azimuth of each retarder is a sinusoid, the detected intensity,  $I_d$ , contains an infinite number of harmonics whose amplitudes depend on Bessel functions,  $J_k(\delta)$ , of the modulation amplitude. Thus,

$$\begin{aligned}
\sin(\delta_i) &= 2 \sum_{n=0}^{\infty} J_{2n+1}(\delta_{0i}) \cos(2n+1)\omega_i t \\
\cos(\delta_i) &= J_0(\delta_i) + 2 \sum_{n=1}^{\infty} (-1)^n J_{2n}(\delta_i) \cos 2n\omega_i t
\end{aligned} \tag{53}$$

The relationships for the elements,  $f_{ij}$  for the bistatic matrix,  $\sigma_{bi}$  are formed by a unique combinations of the frequencies  $\omega_i$ ,  $i = [1, 4]$ .

$$\begin{aligned}
f_{11} &= \text{DC} & f_{12} &= 2\omega_1 & f_{13} &= \omega_1 \pm \omega_2 & f_{14} &= \omega_1 \pm 2\omega_2 \\
f_{21} &= 2\omega_4 & f_{22} &= 2\omega_1 \pm 2\omega_4 & f_{23} &= \omega_1 \pm \omega_2 \pm 2\omega_4 & f_{24} &= \omega_1 \pm 2\omega_2 \pm 2\omega_4 \\
f_{31} &= \omega_3 \pm \omega_4 & f_{32} &= 2\omega_1 \pm \omega_3 \pm \omega_4 & f_{33} &= \omega_1 \pm \omega_2 \pm \omega_3 \pm \omega_4 \\
& & f_{34} &= \omega_1 \pm 2\omega_2 \pm \omega_3 \pm \omega_4 \\
f_{41} &= 2\omega_3 \pm \omega_4 & f_{42} &= 2\omega_1 + 2\omega_3 \pm \omega_4 & f_{43} &= \omega_1 \pm \omega_2 \pm 2\omega_3 \pm \omega_4 \\
& & f_{44} &= \omega_1 \pm 2\omega_2 \pm 2\omega_3 \pm \omega_4
\end{aligned} \tag{54}$$

However, if particles being measured are spherical, matrix elements  $f_{13}, f_{14}, f_{23}, f_{24}, f_{31}, f_{32}, f_{41}$ , and  $f_{42}$  reduce to zero.

## 5.0 INSTRUMENT DESIGN

When a polydisperse collection of spherical particles whose PSDF has particle diameters lying between a minimum diameter  $D_0$  and a maximum diameter  $D_{max}$  is illuminated by a polarized laser of wavelength  $\lambda$  and radiant power  $P_i$ , the scattered received power  $P_r$  at a scattering angle  $\theta$  is given by (Refs. 29, 30)

$$P_r(\theta) = \frac{P_i}{(4\pi)^3} \int_{D_0}^{D_{max}} \int_V \frac{\lambda^2 G_i(\hat{i}) G_r(\hat{O})}{R_2^2} \sigma_{bi}(\tilde{m}, D, \theta) n(D) dD dV \quad (55)$$

where  $\theta$  is defined by

$$\theta = \pi - \arccos \frac{\hat{O} \cdot \hat{i}}{|\hat{O}| |\hat{i}|} \quad (56)$$

$\hat{i}$  and  $\hat{O}$  being the direction vectors from the illuminating source to the detector as shown in Figure 3.

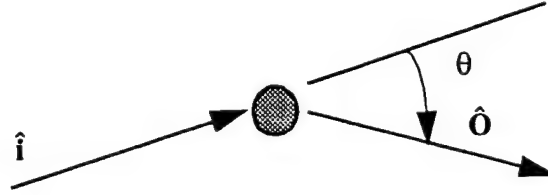


**Figure 3**  
**The Relation Between the Incident Source Position Vector and the Scattered Detector Vector**

$G_i(\hat{i})$  and  $G_r(\hat{O})$  are the gain functions for the incident and scattered power.

The first order multiple scattering model is used to correct for the presence of particles in the incident and scattered light paths. This is done by calculating the optical path,  $\gamma$ , from the illumination source to the particle sample volume and the optical path,  $\gamma_2$ , from the particle sample volume to the detector. Thus, the correction factor has the form of

$$e^{-(\gamma_1 + \gamma_2)} \quad (57)$$

and modifies the received power,  $P_r$ ;

$$P_r = \frac{P_i}{(4\pi)^3} \int_{D_0}^{D_{max}} \int_V \frac{\lambda^2 G_i(\hat{i}) G_r(\hat{O})}{R_2^2} \sigma_{bi}(\tilde{m}, D, \theta) n(D) e^{-(\gamma_1 + \gamma_2)} dD dV \quad (58)$$

If a fixed detector is placed as a fixed scattering angle,  $\theta_f$ , so the received power,  $P_r$  is

$$P_r(\theta_f) = \frac{P_t}{(4\pi)^3} \int_V \int_{D_o}^{D_{\infty}} \frac{\lambda^2 G_t(\hat{i}) G_r(\hat{O}_f)}{R_2^2} \underline{\sigma}_{bi}(\tilde{m}, D, \theta) n(D) e^{-(\gamma_1 + \gamma_2)} dD dV, \quad (59)$$

we can approximately cancel out the effects of the optical distance,  $\gamma_i$ , provided that the sampling volume is small and the distribution of particle sizes in the media is uniform. If the sampling volume is given by

$$V_c = 1.206 \frac{R_1^2 R_2^2 \theta_1 \theta_2 \phi_1 \phi_2}{[R_1^2 \phi_1^2 + R_2^2 \phi_2^2] \sin \theta_s} \quad (60)$$

where the half-power beamwidths for the laser are  $\theta_1, \phi_1$  and for the detector,  $\theta_2, \phi_2$ . The scattering angle,  $\theta_s$ , must be greater than both of the half-power beamwidths.

Now, making these assumptions allows us to move the optical path correction out of the integrand. The new equation for the received power,  $P_r$  is

$$P_r(\theta) = \frac{P_t}{(4\pi)^3} e^{-(\gamma_1 + \gamma_2)} \int_V \int_{D_o}^{D_{\infty}} \frac{\lambda^2 G_t(\hat{i}) G_r(\hat{O})}{R_2^2} \underline{\sigma}_{bi}(\tilde{m}, D, \theta) n(D) dD dV \quad (61)$$

and for the fixed detector,

$$P_r(\theta_f) = \frac{P_t}{(4\pi)^3} e^{-(\gamma_1 + \gamma_2)} \int_V \int_{D_o}^{D_{\infty}} \frac{\lambda^2 G_t(\hat{i}) G_r(\hat{O}_f)}{R_2^2} \underline{\sigma}_{bi}(\tilde{m}, D, \theta) n(D) dD dV. \quad (62)$$

Thus, taking the ratio of the received power,  $P_r$  of a variable positioned detector to the received power,  $P_f$ , of the fixed detector approximately cancels out the optical path effects by taking the ratio of the received power,  $P$ , and the fixed detector power,

$$\frac{P_r(\theta)}{P_r(\theta_f)} = \frac{\int_V \int_{D_o}^{D_{\infty}} \frac{\lambda^2 G_t(\hat{i}) G_r(\hat{O})}{R_2^2} \underline{\sigma}_{bi}(\tilde{m}, D, \theta) n(D) dD dV}{\int_V \int_{D_o}^{D_{\infty}} \frac{\lambda^2 G_t(\hat{i}) G_r(\hat{O}_f)}{R_2^2} \underline{\sigma}_{bi}(\tilde{m}, D, \theta) n(D) dD dV}. \quad (63)$$

If the illuminating source is a narrow laser beam, the gain function for the laser is

$$G_t(\hat{i}) = \frac{2}{\pi W_o} \exp\left(-\frac{\rho^2}{W_o^2} - \frac{k^2 W_o^2 \sin^2 \theta}{2}\right) \quad (64)$$

And, the gain function for the receiver is

$$G_r(\hat{i}) = \left( \frac{4\pi\eta_r A_r}{\lambda^2} \right) (\exp(\{-(\log 2)[(2\theta/\theta_2)^2 + (2\phi/\phi_2)^2]\})). \quad (65)$$

The above equations are valid for a randomly distributed, polydisperse collection of spherical particles. This equation takes into account the aperture sizes of the laser and receiver, attenuation of the incident laser beam and scattered light, and the particle size distribution.

The time required to acquire a statistically representative sample is  $\Delta t$ . However, the mass seen by the detector during some sampling time interval,  $\Delta t$ , is the expected mean mass flux,  $\langle \dot{m} \rangle$  and the contribution by the moment to moment fluctuations in the mass flux,  $\langle \dot{m} - \langle \dot{m} \rangle \rangle$ . The mass sampled,  $m_s$ , in this time interval,  $\Delta t$ , would be

$$m_s = \int_{\Delta t} \langle \dot{m} \rangle dt \pm \left( \lim_{\Delta t \rightarrow t_B} \int_{\Delta t} \langle \dot{m} - \langle \dot{m} \rangle \rangle dt = 0 \right) \quad (66)$$

where  $t_B$  is the motor burn time. All ambiguity can be canceled out by measuring the total mass. Because of the fluctuations in the mass flux,  $\dot{m} = \langle \dot{m} \rangle \pm \langle \dot{m} - \langle \dot{m} \rangle \rangle$ , the sampling time may be a significant portion of the motor burn time,  $t_B$ . It may be possible to determine a sampling interval,  $\Delta t$  that is a fraction of this value. However, it may not be possible to know  $\Delta t$  before the motor burns out. The criteria for  $\Delta t$  would mean the minimizing of  $\langle \dot{m} - \langle \dot{m} \rangle \rangle$ . The accumulated intensity,  $I_a$  is related to the sampled intensity,  $I_s$  by

$$I_a = \sum_{T_s/(\Delta t)} I_s. \quad (67)$$

The equivalent intensity,  $I_{eq}$ , is related to the accumulated intensity,  $I_a$ .

$$I_{eq} = \frac{I_a}{T_s} \Delta t \quad (68)$$

where  $t_s$  is the total sampling time. In the derivations that follow, all calculations are made with the equivalent intensity in mind.

## 6.0 TENTATIVE OPTICAL INSTRUMENT DESIGN

The schematic in Figure 4 incorporates all the material discussed so far. After passing through the Electro-Optical Modulator, the laser beam enters the Sample Volume Control. In conjunction with the Coherence detector, the Sample Volume Control adjusts the beam diameter in order to maintain the validity of the first order scattering approximation. Then, the compensated beam is split into two equal intensity paths. One path passes through the Particle Stream and is scattered by the particles. The line of sight portion passes into the Coherence Detector where the particle density is determined. The resultant signal is passed back to the Sample Volume Control. A Photo Diode Array scans a selected portion of the scattered beam. The signal from the Photo Diode Array is used to determine the PSDF.

Array scans a selected portion of the scattered beam. The signal from the Photo Diode Array is used to determine the PSDF.

The second path passes through the Polarization State Generator (PSG). The elliptical beam passes through the Particle Stream. The fixed angle Polarization State Analyzer (PSA) determines the change in polarization of the light scattered into it. The resultant signal is used to determine the bulk optical properties. The apparent temperature of the particles is measured by the Optical Pyrometer.

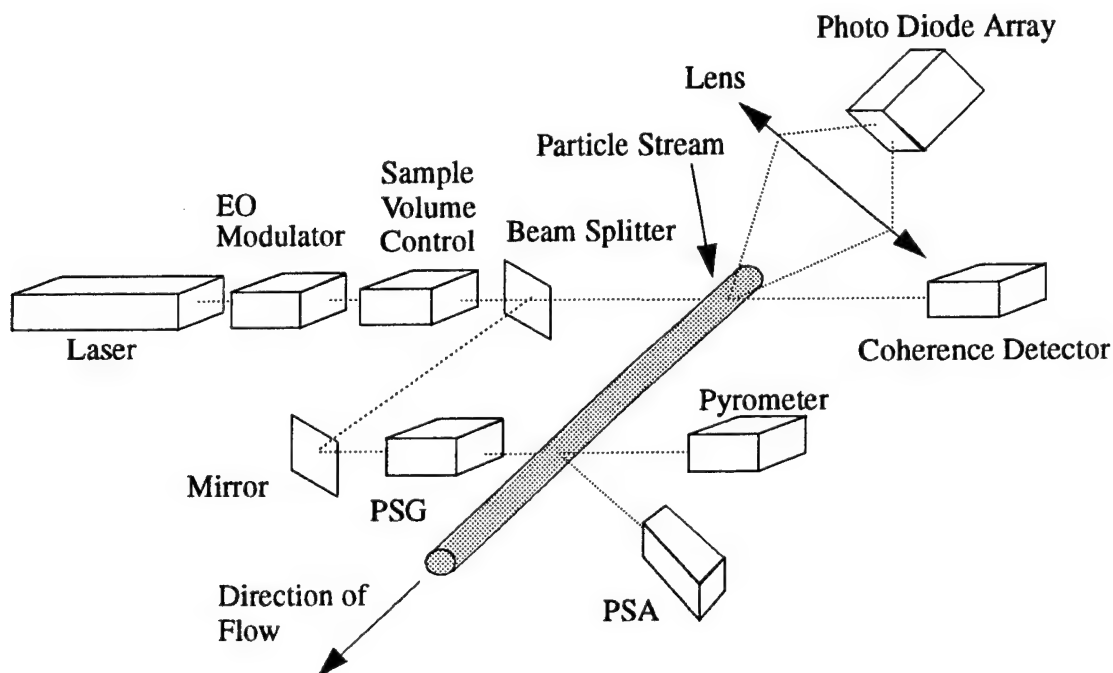


**Figure 4**  
**The *In Situ* Particle Probe, Based upon the Presented Theoretical Discussions**

## 7.0 FIRST ORDER DETERMINATION OF THE PARTICLE SIZE DISTRIBUTION FUNCTION (PSDF)

As the literature demonstrates, the extraction of the PSDF is very difficult (Refs. 31 to 67). The difficulty lies in the similarity and very low intensity of the scattered intensity patterns of the sub-micron sized particles. As the following pages will show, it is possible to determine the PSDF by the use of a Genetic Algorithm. First, there will be some simplifying assumptions made about Equation [63].

Referring back to Equation [55], let

$$\frac{P_t}{(4\pi)^3} \cdot \frac{\lambda^2 G_t(\hat{\mathbf{i}}) G_r(\hat{\mathbf{O}})}{R^2} = 1 \quad (69)$$

and neglecting the compensating detector measurements made by  $P_f$  Equation [63] becomes

$$P_r = \int_V \sigma_{bi}(\tilde{\mathbf{m}}, D, \hat{\mathbf{O}}, \hat{\mathbf{i}}, \tau) n(D) dD \quad (70)$$

Further, the assumption is made that measurements are made at discrete angles for discrete particle sizes. This transforms Equation [70] into

$$P_d(\theta_j) = \sum_{i=1} \sigma_{bi}(D_i, \theta_j, \tilde{\mathbf{m}}, \lambda) \bullet n(D). \quad (71)$$

This equation represents the power scattered into a detector located at the scattering angle,  $\theta$ , by a continuum of particles whose smallest diameter is  $D_0$  and largest is  $D_{max}$ . If a single power measurement is taken at one angle, there would be an infinite number of possible PSDFs whose intensities matched at that angle. Ideally, measurements taken at an infinite number of angles would define the PSDF, but this is not feasible from an experimental viewpoint. Where  $\sigma_{bi}$  is the  $M \times N$  matrix ( $M = 64$ ,  $N = 100$ ) of bistatic scattering coefficients and  $PSDF(D)$  is the  $n = 100$  element column vector containing the number of particles of diameter  $D_i$ . Calculation of the rank of  $\sigma_{bi}$  is of 33. The condition number (CN) (Refs. 45 - 47) of  $\sigma_{bi}$ , which is a measure of the sensitivity of the solution to perturbations in the  $\mathbf{I}$ , is  $2.1393e+17$ . Thus,

$$\frac{\|\Delta \hat{\mathbf{n}}(D)\|}{\|\hat{\mathbf{n}}(D)\|} \leq \text{cond}(\sigma_{bi}) \frac{\|\Delta \hat{\mathbf{l}}(\theta)\|}{\|\hat{\mathbf{l}}(\theta)\|} = \frac{\max(s) \|\Delta \hat{\mathbf{l}}(\theta)\|}{\min(s) \|\hat{\mathbf{l}}(\theta)\|} = (2.1393 \times 10^{17}) \frac{\|\Delta \hat{\mathbf{l}}(\theta)\|}{\|\hat{\mathbf{l}}(\theta)\|} \quad (72)$$

where  $s$  is the diagonal matrix containing the eigenvalues of  $\sigma_{bi}$ . This means that in the inversion process small numerical errors are multiplied by large factors and may cause all significant figures to be lost. Thus,  $\sigma_{bi}$  is a singular matrix. Figure 5 shows the eigenvalues,  $S_{ii}$ , of  $\sigma_{bi}$  where singular values,  $S_{ii}$ , of the matrix,  $\sigma_{bi}$ , are plotted in max to min order.

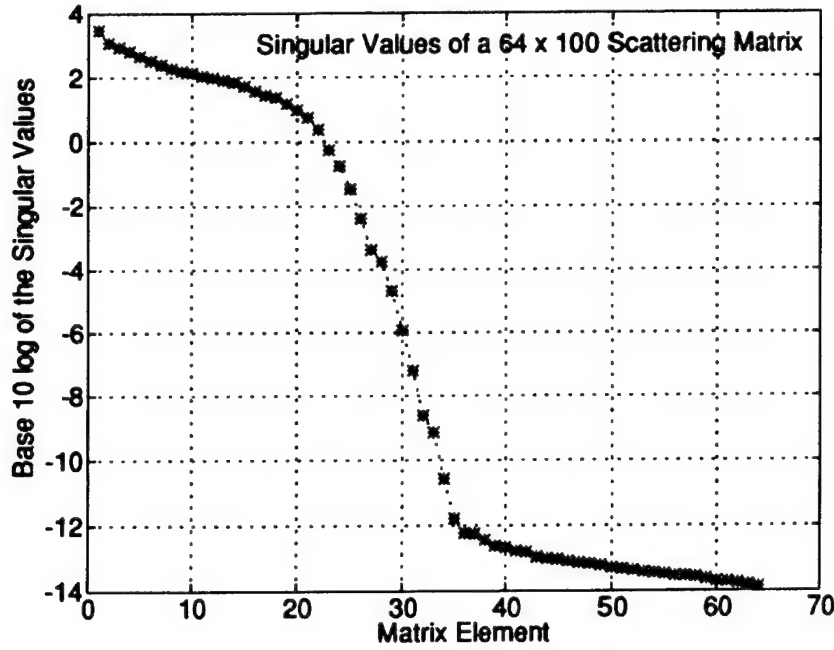


**Figure 5**  
**Singular Values of a 64 by 100 Scattering Matrix**

Consequently, the emphasis was shifted from solving the inverse problem,

$$n(D) = \sum \sigma_{bi}^{-1} \cdot I(\theta)^T \quad (73)$$

to finding a suitable optimization method that could search for a solution of the mean-squared-error (MSE) function,

$$|\hat{e}|^2 = \left( \hat{P}_d - \sum_{i=1}^N c_i \sigma_{bi}(D_i) \right)^2 \quad (74)$$

A study was performed to determine those angles for a given incident polarization that were least sensitive to variations in the complex index of refraction. For the study, two incident polarizations were chosen. The two incident polarizations, parallel and perpendicular to the scattering plane, are related to the Stokes vectors by (Ref. 23)

$$I_s = f_{11} \cdot I_0 + f_{12} \cdot Q_0 \quad Q_s = f_{21} \cdot I_0 + f_{22} \cdot Q_0 \quad Q_0 = I_0 \quad U_0 = V_0 = U_s = V_s = 0 \quad (75)$$

where

$$(f_{11} + f_{12}) = (f_{21} + f_{22}) = |S_2|^2 \quad (76)$$

for the parallel polarization, and



$$I_s = f_{11} \cdot I_0 - f_{12} \cdot Q_0 \quad Q_s = f_{21} \cdot I_0 - f_{22} \cdot Q_0 \quad Q_0 = -I_0 \quad U_0 = V_0 = U_s = V_s = 0 \quad (77)$$

where

$$(f_{11} - f_{12}) = (f_{21} - f_{22}) = |S_1|^2 \quad (78)$$

for the perpendicular component.

Four particle sizes were chosen to represent the range of particles to be measured. In each Mie plot for a given particle, the real part of the complex index is fixed at 1.7 (Ref. 6), while the imaginary part was varied from 0.001 to 0.1 with succeeding values overlaid. In Figure 6, the polarization is perpendicular to the scattering plane.

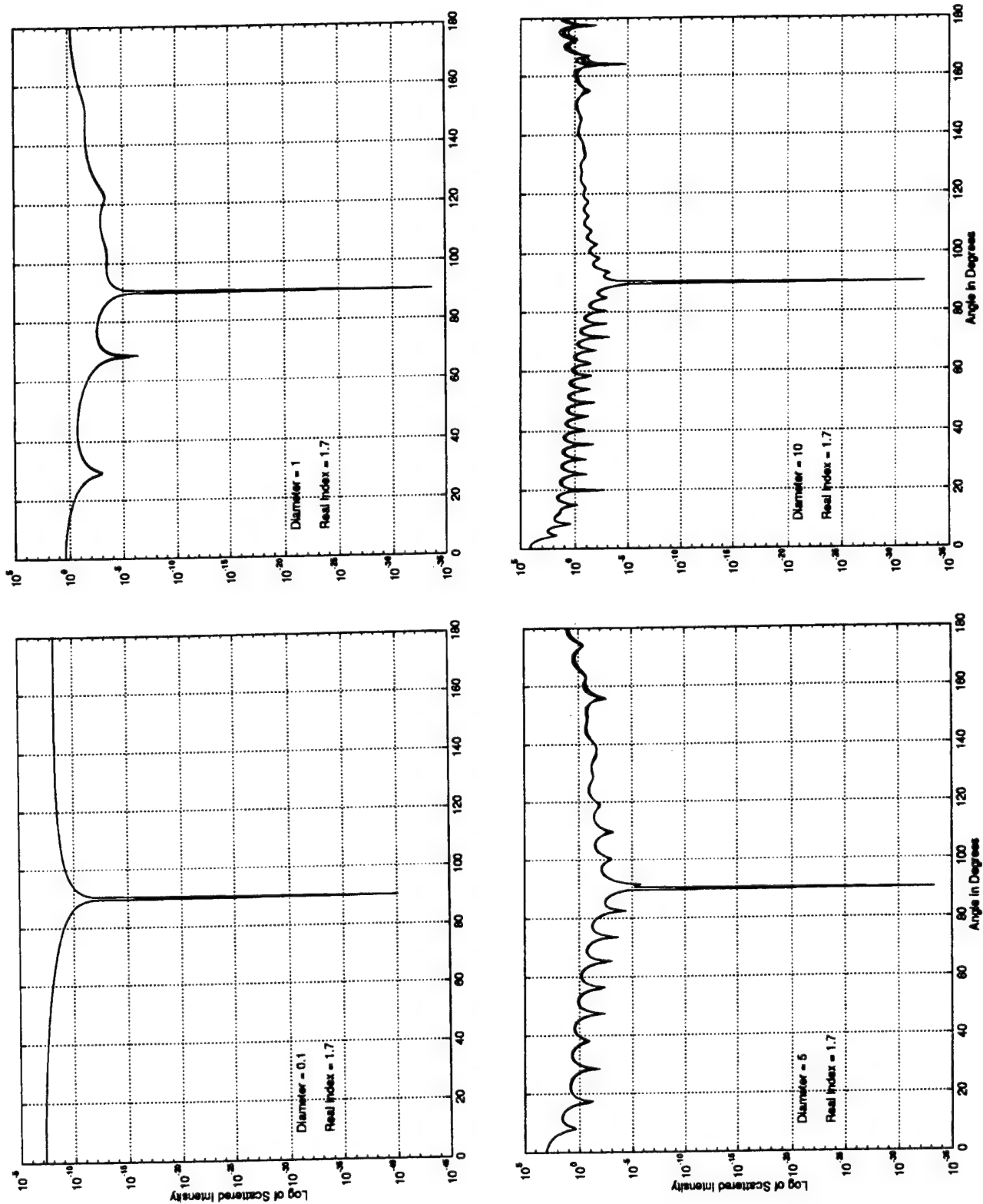


**Figure 6**  
**Intensity versus Angle Scattering for Perpendicular Polarization,  $|S_1|^2$**

The four plots in Figure 6 show that the Mie scatter is most sensitive to variations of the imaginary index for the angles between  $140^\circ$  to  $180^\circ$ . The next four plots of Figure 7 show the Mie scattering for parallel polarization. As can be seen in the plots for the 5- and 10- $\mu\text{m}$  particles, the Mie scatter is sensitive to variations in imaginary index for the angles  $20^\circ$  to  $85^\circ$  and  $140^\circ$  to  $180^\circ$ . The plots from Figure 6 show that the forward angles are least sensitive to variations in the imaginary part of the complex index of refraction when the polarization is perpendicular to the scattering plane. The range of angles chosen for the first order calculations are from  $5^\circ$  to  $37.5^\circ$ , with  $0.5^\circ$  increments.

Several optimization methods that could find the global minima were studied, including the Levenberg-Marquardt Least Squares method, Nedler and Mead downhill simplex, Stimulated Annealing, Neural Networks, and Genetic Algorithms (Refs. 46 - 51). The details of the results will not be presented here; there will be a very brief statement about the outcome of the studies. The Levenberg-Marquardt Least Squares method, Nedler and Mead downhill simplex performed about equally. Performing multiple trials, the average solution would lie near the true answer; the standard deviation was quite large, about fifty percent of the average value. The cause for this uncertainty is believed to be a flatness in the solution plane near the correct answer. This assumes that these algorithms can resolve the large particle size correctly, which they seem to do. As for Stimulated Annealing, the outcomes were similar to those previously mentioned. As an added note, Simulated Annealing uses Boltzman statistics (Refs. 49, 50)

$$p(x) = e^{[-(f(x_j) - f(x_{j-1})) / (T_j \cdot f(x_{j-1}))]} \quad (79)$$

where the current function value is compared with the proceeding value. The temperature,  $T_j$ , is used as a cooling profile, beginning with an initial temperature,  $T_0$ , and is driven by the iteration count,  $j$ , and the total number of iterations is  $J$ ,

$$T_j = T_0 \left(1 - \frac{j}{J}\right)^\alpha \quad (80)$$

randomly searches the solution space and in an almost infinite amount of time can converge infinitely close to the solution. Usually, a separate method is used to converge to the solution after a finite number of iterations. A survey of both feedforward and recurrent Neural Network types indicated that Neural Networks are great classifying engines and at approximating functions. Given a predefined input, a Neural Network will present a predefined output. The network can be taught to recognized many predefined inputs and can perform a form of interpolation when presented an input that is a pertubation of one of the predefined inputs. Unfortunately, there is no guarantee that the interpolated output will be meaningful. Thus, the network needs to be taught to recognize almost all of the possible inputs one expects. This would require a tremendous amount of time and computer memory. For example, if there were twenty inputs to the networks where the intensity measurements,  $I(\theta)$ , the number of possible combinations of neurons, connections, layers and transfer functions are on the order of 100 billion.

From these studies, it was clear that what was needed was a way to stochastically explorer the solution space while being able to simultaneously converge to a solution. The Genetic Algorithm seemed to be the perfect choice.

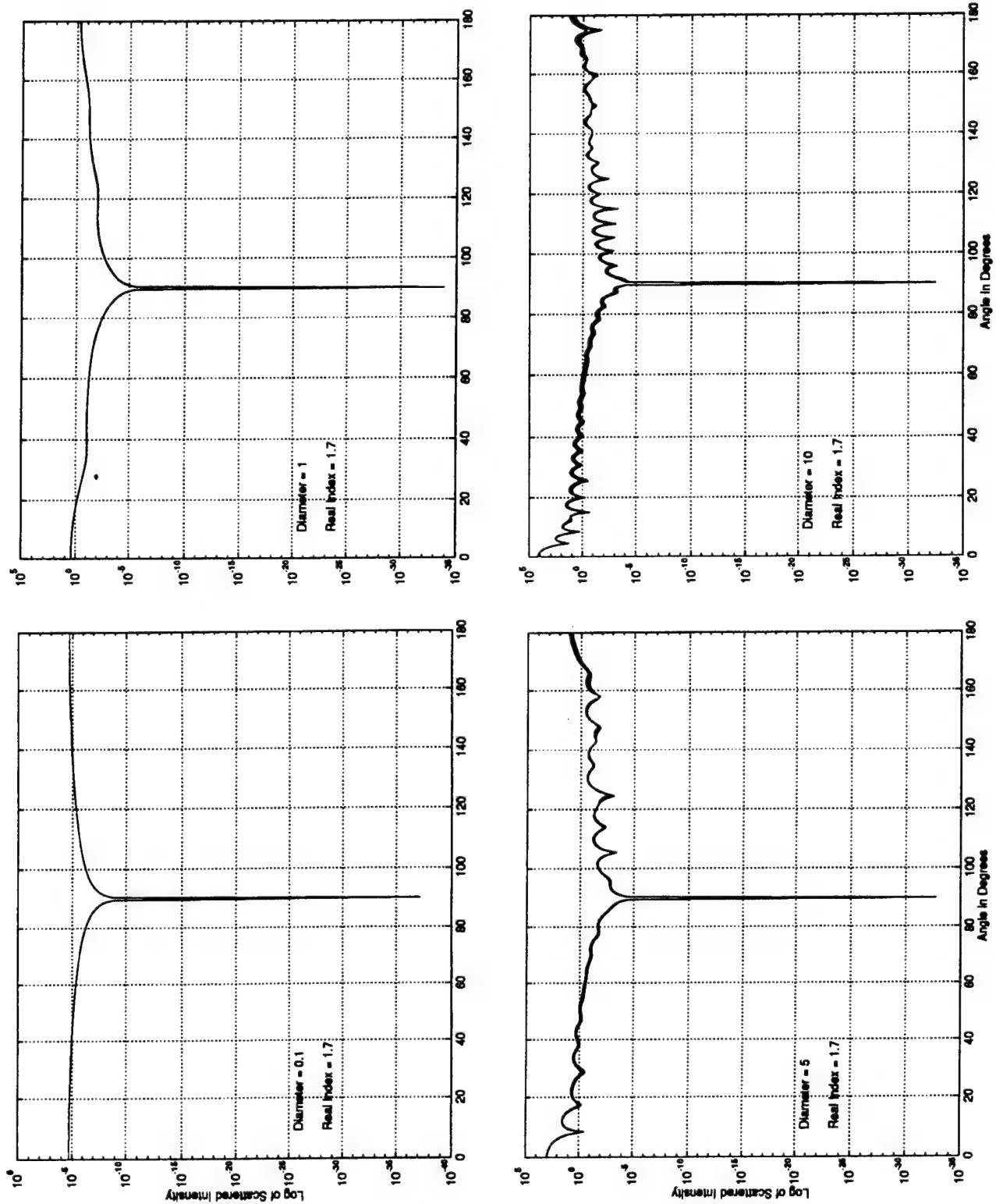


Figure 7  
Intensity versus Angle Scattering for Parallel Polarization,  $|S_2|^2$

Suppose that the optimal solution is desired for a given problem. It is irrelevant if the solution is a scalar or a vector; in either case, the solution can be given in the form of a vector. For example, if the solution is a scalar,  $q$ , the vector form of  $q$  would be,

$$q = \sum_{i=1}^N a_i \times 10^i + \sum_{i=1}^M b_i \times 10^{-i} \quad (81)$$

and for the vector,  $\hat{x}$ , the form is

$$\hat{x} = [x_1, x_2, \dots, x_n]. \quad (82)$$

In either case, the solution space consists of a set of 1 x m-dimensional vectors. Suppose that the function to be optimized is

$$\epsilon = |f(\hat{x}) - \vec{C}| \quad (83)$$

where  $f(\hat{x})$  is some vector function and that  $\vec{C} = [c_1, c_2]$  is a vector constant. The goal is to make  $\epsilon$  as small as possible. This idea is illustrated in Figure 8: There are two trial solutions,  $\hat{a}$  and  $\hat{b}$ . It is obvious that the solution lies somewhere between them. Thus, one would like to combine them to provide another set of solutions that lie closer to the optimal value,  $\vec{C}$ . A genetic algorithm (GA) does this by swapping vector elements. But constant reapplication of element swapping may lead to solutions that don't converge, such as  $\hat{d}$ . This problem is overcome by the occasional perturbation of a vector element.

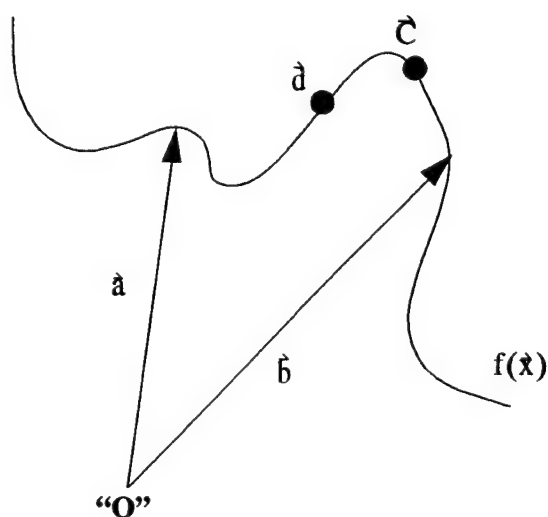


**Figure 8**  
**Trial Solutions  $\hat{a}$  and  $\hat{b}$  Converging to  $\vec{C}$**

The GA evaluates a set of trial solutions and usually selects those with above average performance. From the chosen trial solutions, some trial solution pairs are selected for element swapping by an operation called crossover, while other single trial solutions have some of their elements perturbed by the mutation operator (the operation that is used is determined by a preset probability,  $p_{op}$ ) (Refs. 68 - 73).

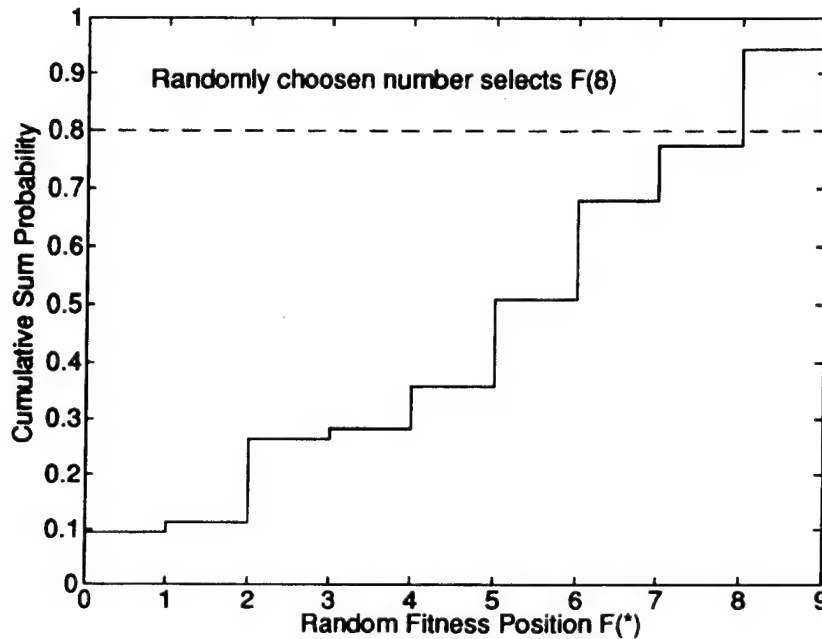
The GA randomly selects trial solutions, but the probability of being selected is based upon the trial solution's relative fitness,  $p$ ,

$$p(\mathbf{x}_k) = \frac{f(\mathbf{x}_k)}{\sum f(\mathbf{x})}. \quad (84)$$

The set of  $p$ 's form a probability distribution in which the most fit solutions have a larger probability. Because the set of fitness values may be quite small,  $p_j \ll 1$ , the GA uses the cumulative sum probability of the fitness values,  $csp$

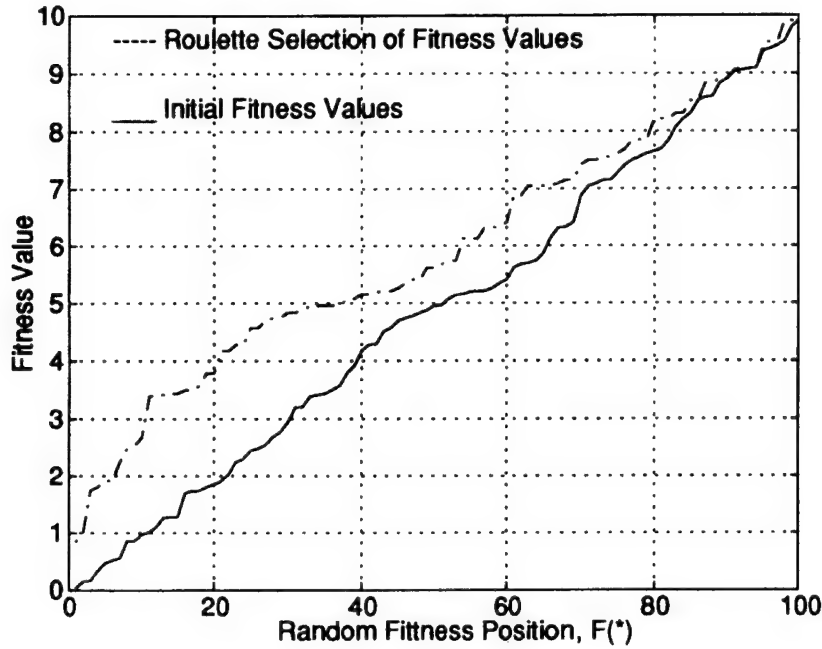
$$csp_j = \left( \sum_{i=1}^j p_i \right) / \sum p. \quad (85)$$

Figure 9 shows the  $csp$  and a randomly chosen trial solution.



**Figure 9**  
**Cumulative Sum and Random Selection**

The standard GA is a hill climber; it looks for the largest value of  $\epsilon$ . This can be seen in Figure 10. Larger values of the fitness function are selected more often than the smaller ones.



**Figure 10**  
**Larger Values are Selected More Often**

To make the GA useful for solving the MSE, it was redesigned to find the global minima. This was accomplished by taking the complement of the  $csp$ , that is

$$qcsp_j = 1 - \left\{ \left( \sum_{i=1}^j p_i \right) / \sum p \right\} . \quad (86)$$

The first tests were performed with a minima seeking combinatorial GA (CGA). The operators for mutation and crossover are shown below. For mutation there is:

a) Uniform mutation, which replaces the chosen element with a value lying somewhere between the lower,  $l_{(k)}^{S_t}$ , and upper,  $u_{(k)}^{S_t}$ , bounds. The superscript,  $S_t$ , designates that these bounds are the current values but may change as desired. Also, each element may have a unique lower and upper bound.

$$v_k^{t+1} = l_{(k)}^{S_t} + r(u_{(k)}^{S_t} - l_{(k)}^{S_t}) \quad r \in [0, 1) \quad (87)$$

b) Boundary mutation replaces the vector element with either the lower bound or the upper one.

$$v_k^{t+1} = \begin{cases} l_{(k)}^{S_t} & \text{if a random digit is 0} \\ u_{(k)}^{S_t} & \text{if a random digit is 1} \end{cases} \quad (88)$$

c) **Bit Mask controlled mutation.** A randomly generated bit mask selects which vector elements are to be altered. Uniform and boundary mutation operators operate on only one element; a randomly generated bit mask operates on more than one element simultaneously.

$$M_b = \langle k_1, k_2, \dots, k_n \rangle, k_i \in [0,1] \quad v_k^{t+1} = (\text{your favorite mutation operator}) \quad (89)$$

Crossover operators follow a similar pattern. Crossover occurs when two selected trial solutions exchange parts of their corresponding vector elements to produce two “child” vectors. There are many ways to perform crossover; the method chosen reflects the type of problem being solved. There are two kinds of crossover operators: Operators that perform combinatoric sharing, and operators that perform map contraction.

Three operators are combinatoric in nature:

a) **One-Point Crossover.** The two selected vectors exchange corresponding vector sub-arrays. Where the sub-arrays begin depends on a randomly chosen index,  $k$ . The results are two children.

Parent 1	1	0	1	1	0	0	1	0
Parent 2	0	1	1	0	1	0	0	1
Child 1	1	0	1	1	1	0	0	1
Child 2	0	1	1	0	0	0	1	0

**Figure 11**  
**One-Point Crossover**

b) **Two-Point Crossover** is a more sophisticated version of One-Point Crossover. Two randomly chosen indexes are used to define the beginning of the vector sub-arrays. Care is taken to insure that the two indexes,  $k_i, k_j$ , aren't equal.

Parent 1	1	0	1	1	0	0	1	0
Parent 2	0	1	1	0	1	0	0	1
Child 1	1	0	1	0	1	0	0	0
Child 2	0	1	1	1	0	0	1	1

**Figure 12**  
**Two-Point Crossover**



c) Bit Mask Controlled Crossover. Similar to Bit Masked Mutation, except that here elements are exchanged between the parents..

Parent 1	1	0	1	1	0	0	1	0
Parent 2	0	1	1	0	1	0	0	1
Bit Mask	0	1	0	0	1	1	0	1
Child 1	1	1	1	1	1	0	1	0
Child 2	0	0	1	0	0	0	0	1

**Figure 13**  
**Bit Masked Crossover**

Naturally the question arises, if the GA can develop solutions using these operators, can potential solutions be destroyed? The answer is yes. The rate of growth of a solution and the probability of its survival have been described in terms of a schemata,  $S$ . A schemata is a template of values. An example is

$$S = [34, *, 3, 11, *, 0] \quad (90)$$

where \* means don't care, the other values are fixed. The range the values can take depends on the cardinality of the alphabet being used. For the above example, the cardinality is 34; thus, there are

$$(k + 1)^l = (34 + 1)^6 \quad (91)$$

possible schema for a solution vector with  $l$  elements. The schemata,  $S$ , contains  $\delta_s$  elements; the probability,  $p_d$ , of its destruction after all the applied operation is

$$p_d = \frac{\delta_s(S)}{(l - 1)} \quad (92)$$

the probability for survival,  $p_s$ , is

$$p_s = 1 - p_d \quad (93)$$

With the probability of crossover,  $p_c$ , and mutation,  $p_m$ , occurring,  $p_s$  becomes

$$p_s \geq 1 - p_c \frac{\delta_s(S)}{(l - 1)} - (1 - p_m)^{o(S)} \quad (94)$$

where  $o(S)$ , the number of fixed positions, is the order of the schemata,  $S$ .

Thus, if the schemata fitness at iteration,  $t$ , is defined as the average fitness of all the trial solutions matched by the schema,  $S$ , then

$$f(S) = \left( \sum_{j=1}^{\eta(S,t)} f(S \in \Phi) \right) / (\eta(S, t)) \quad (95)$$

where  $f(S)$  is the fitness value of those vectors containing the schemata,  $S$ , and the number of schemata present in the population is given by  $\eta(S, t)$ .

The number of trial solutions containing schemata,  $S$ , at iteration  $t+1$  is

$$\eta(S, t+1) = \eta(S, t) \cdot nf(S) / \sum f_j \quad (96)$$

where  $n$  is the total number of potential solutions and  $\sum f_j$  is their sum. Let the average value of the fitness be

$$\bar{f} = \sum f_j / n. \quad (97)$$

Then, Equation [96] becomes

$$\eta(S, t+1) = \eta(S, t)(f(S)/\bar{f}). \quad (98)$$

Define  $\tau$  as the growth factor for schemata,  $S$ , Equation (98) becomes

$$f(S) = (1 + \tau)\bar{f} \rightarrow \tau = (f(S) - \bar{f})/\bar{f}. \quad (99)$$

With  $\tau > 0$  for above average schemata and  $\tau < 0$  for below average schemata, the growth equation can be written as

$$\eta(S, t) = \eta(S, 0)(1 + \tau)^t. \quad (100)$$

This geometric progression equation shows that the number of above average schema grows exponentially.

Now, incorporating the probability of survival into these equations results in the expected number of schemata,  $S$ , at iteration  $t+1$  to be

$$\eta(S, t+1) \geq \eta(S, t) \frac{f(S)}{\bar{f}} \left\{ 1 - p_c \frac{\delta_s(S)}{(l-1)} - o(S)p_m \right\}. \quad (101)$$

For the purpose of the next set of calculations, the schemata,  $S$ , consisted of the values zeros thru 60. The length,  $l$ , of  $S$  was set to 1.

The equation the CGA worked to solve was Equation [74]. The results of the combinational GA were encouraging, as Figure 14 indicates.

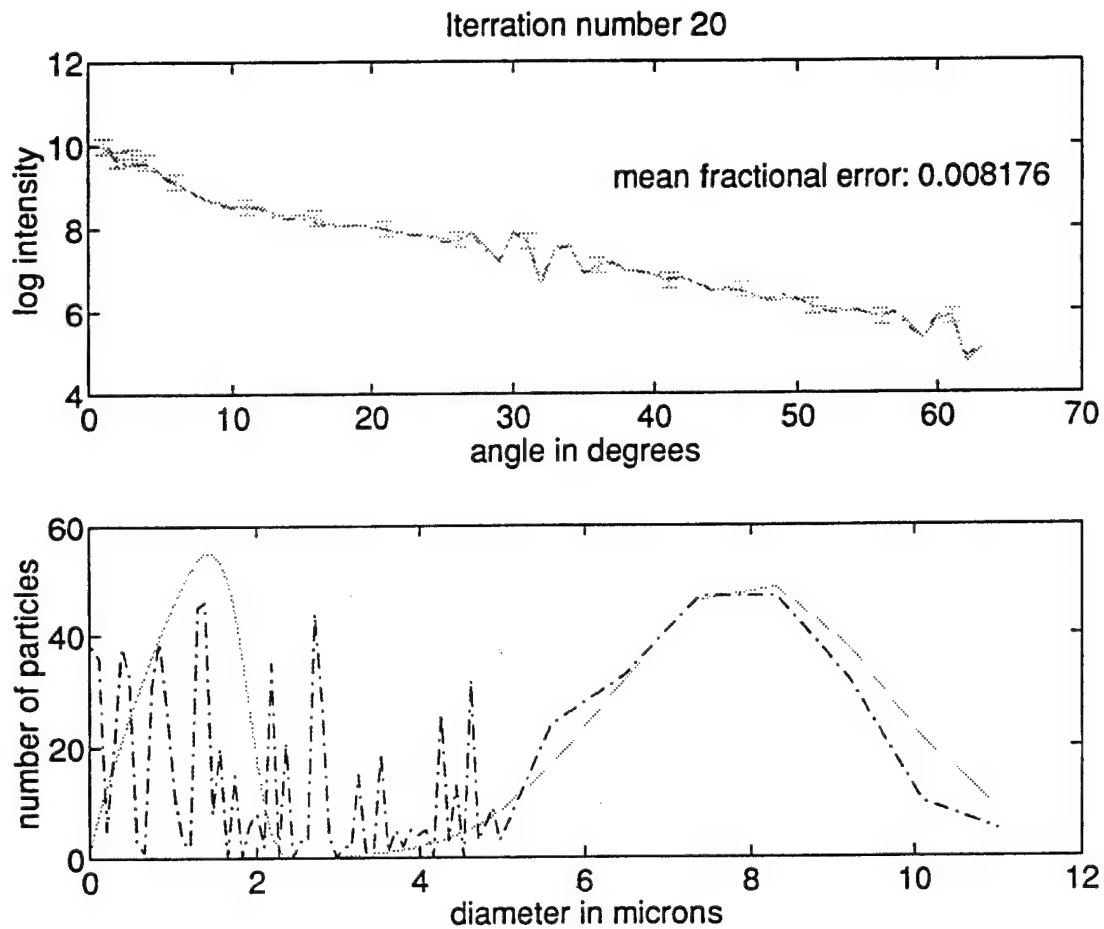


**Figure 14**  
**First Results Using CGA**

The figure shows the results after 20 iterations. Further iterations failed to improve convergence. The test distribution was bimodal. The GA resolved the larger particles quite well, but the smaller particles sizes have a great deal of uncertainty. Note that the calculated intensity fit the test intensity well. The author believes that the condition number of the Mie scattering matrix was the cause of the error.

Several modifications were made to the CGA, culminating in the Adaptive GA (AGA). Instead of a single crossover operator and mutation operator, the AGA has a battery of operators from which to select. The AGA not only selects the children of the next generation by their performance in the object function but also assigns a fitness value to the operators used. An operator's performance is the amount of improvement in the population for which the operator is responsible. The operator performance figure is determined by adding a decreasing fraction of a fixed number to the ancestors of a child that survives the fitness evaluation. The paradigm is used in Figure 15.

1. Whenever a child is created, record who its parents were and the operator that created it.
2. Whenever a child is created that is better than the best nonmember of the population, give it an amount of credit equal to the amount that its evaluation exceeds the best evaluation.
3. When a child is given credit for having a better evaluation, add a portion of that credit to the credit amounts of the child's parents, then to their parents and so on.
4. To compute the performance of an operator over an interval of a certain length, sum the credit of each child the operator produced in that interval and divide by the number of children.

**Figure 15**  
**Outline of Adaptive Procedure**

The additional mutation and crossover operators used by the AGA are:

(a) Non-uniform mutation, which selects an element for the vector. However, the magnitude of the perturbation is affected by the iteration value. As the iteration value grows, the magnitude of the perturbation decreases. This keeps the GA from making large jumps late in the evaluation.

$$v_k^{t+1} = \begin{cases} v_k^t + \Delta(t, u_{(k)}^{S_t} - v_k^t) & \text{if a random digit is 0} \\ v_k^t - \Delta(t, v_k^t - l_{(k)}^{S_t}) & \text{if a random digit is 1} \end{cases} \quad (102)$$

$$\Delta(t, y) = y(1 - r^{(1-t/T)}) \quad r \in [0, 1)$$

(b) One-Point Arithmetic Crossover. This is the same as the One-point Crossover, except that linear scaling is used to replace the selected sub-array elements.

$$\begin{bmatrix} \hat{v}_{a_k}^{t+1} \\ \hat{v}_{\beta_k}^{t+1} \end{bmatrix} = \begin{bmatrix} \hat{v}_{\beta_k}^t & \hat{v}_{a_k}^t \\ \hat{v}_{a_k}^t & \hat{v}_{\beta_k}^t \end{bmatrix} \begin{bmatrix} a \\ (1-a) \end{bmatrix} \quad (103)$$

where  $a$  is a randomly chosen number;  $0 < a < 1$ .

(c) Two-Point Arithmetic Crossover. This is like Two-Point Crossover, with the linear scaling used in the One-Point Arithmetic Crossover.

$$\begin{bmatrix} \hat{v}_{a_k, \dots, j}^{t+1} \\ \hat{v}_{\beta_k, \dots, j}^{t+1} \end{bmatrix} = \begin{bmatrix} \hat{v}_{\beta_k, \dots, j}^t & \hat{v}_{a_k, \dots, j}^t \\ \hat{v}_{a_k, \dots, j}^t & \hat{v}_{\beta_k, \dots, j}^t \end{bmatrix} \begin{bmatrix} a \\ (1-a) \end{bmatrix} \quad R = \langle 1, 1+1, \dots, s-1, s \rangle \quad (104)$$

(d) Bit Mask Controlled Arithmetic Crossover.

$$M_b = \langle k_1, k_2, \dots, k_n \rangle, k_i \in [0,1] \quad \begin{bmatrix} \hat{v}_{a_{M_b}}^{t+1} \\ \hat{v}_{\beta_{M_b}}^{t+1} \end{bmatrix} = \begin{bmatrix} \hat{v}_{\beta_{M_b}}^t & \hat{v}_{a_{M_b}}^t \\ \hat{v}_{a_{M_b}}^t & \hat{v}_{\beta_{M_b}}^t \end{bmatrix} \begin{bmatrix} a \\ (1-a) \end{bmatrix} \quad (105)$$

(e) Whole Arithmetical Crossover. Replaces the parent vectors with linear scaled children.

$$\begin{bmatrix} \hat{v}_{\alpha}^{t+1} \\ \hat{v}_{\beta}^{t+1} \end{bmatrix} = \begin{bmatrix} \hat{v}_{\beta}^t & \hat{v}_{\alpha}^t \\ \hat{v}_{\alpha}^t & \hat{v}_{\beta}^t \end{bmatrix} \begin{bmatrix} a \\ (1-a) \end{bmatrix} \quad (106)$$

Unfortunately, the AGA was very slow and the results weren't very different from those produced by the combinatoric GA. However, the AGA showed that the Whole Arithmetical Crossover and Non-Uniform Mutation operators were the most effective at evaluating solutions.

Next trials incorporated improvements in the trial solution selection function. The  $qcsp$  is pre-scaled by a Boltzman like distribution function,  $p_{Boltz}$ ,

$$p_{Boltz} = \frac{1}{1 + \alpha \exp(\beta \Delta E)} \quad (107)$$

where  $\alpha$  and  $\beta$  are parameters chosen to maximize GA performance by shifting and scaling the selection curve. The effect of  $\alpha$  and  $\beta$  parameter can be seen in Figure 16.

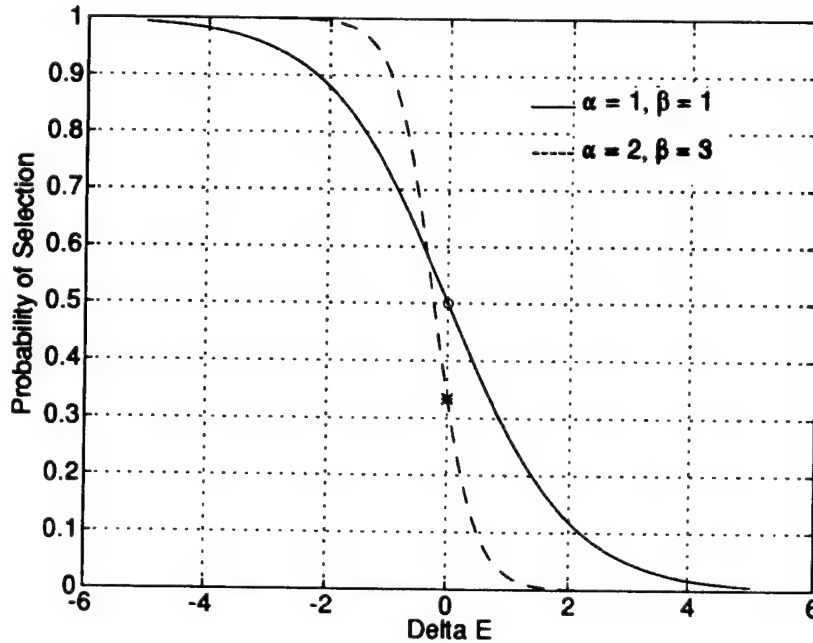


**Figure 16**  
**Comparison of Modified Boltzman to Standard Boltzman Used in Simulated Annealing**

The probability selection rate was increased from 50 percent to about 66 percent by setting  $\alpha$  to 2 and  $\beta$  to 3. The overall effect can be seen in Figure 17. Modified Boltzman improves performances by selecting the smaller solutions more often.

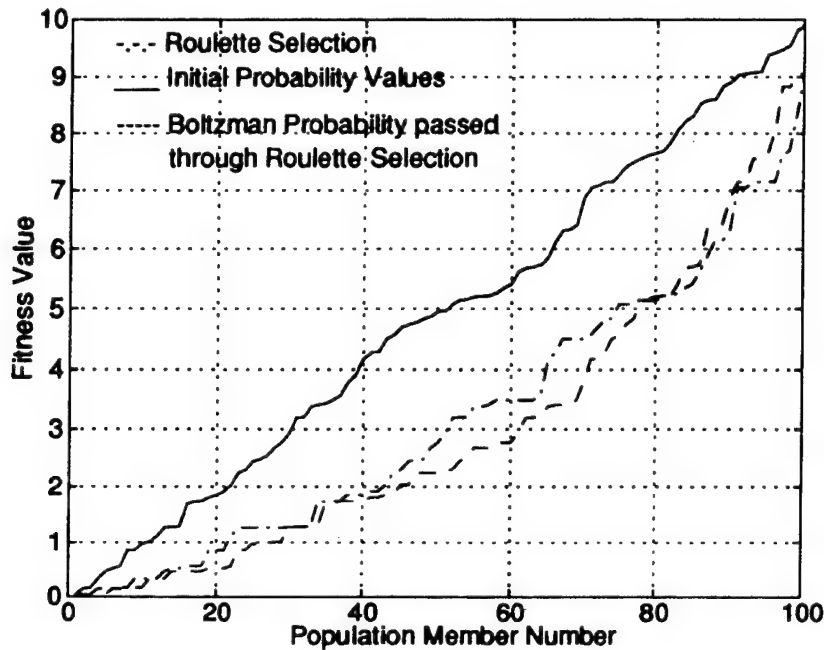


**Figure 17**  
**Comparison of Non-scaled and Scaled Selection Results**

This new GA was designated SAGA for Simulated Annealing Genetic Algorithm. This improved GA was faster but still didn't converge to the desired solutions.

The breakthrough came in transforming the PSDF to the equivalent Integrated Mass Distribution (IMD). The IMD is related to the PSDF by the following integral

$$\text{IMD}(D) = \rho \frac{\pi}{6} \int_0^D x^3 \frac{n(x)}{\int_0^\infty n(x) dx} dx . \quad (108)$$

Figure 18 shows the bimodal IMD used for the next solution trials.

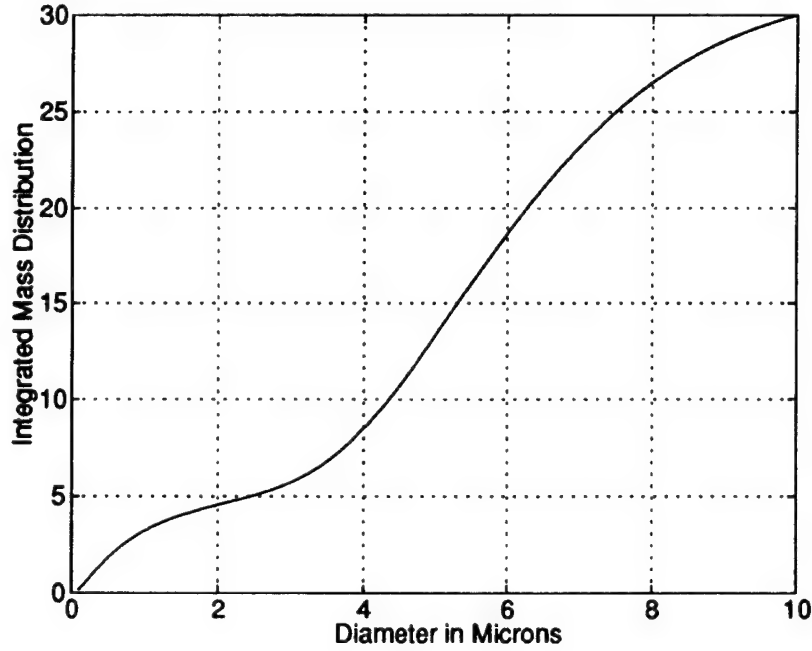


**Figure 18**  
**Bimodal Integrated Mass Distribution**

The elements of the Mie scattering matrix were divided by the particle volume,

$$\chi_{ij} = f_{ij} / \left( \frac{\pi}{6} \rho D_j^3 \right). \quad (109)$$

The scattered intensity equation, Equation [36], becomes

$$I_s = (1 / (k^2 r^2)) \bar{\chi}_{bi} I_i. \quad (110)$$

To further simplify computational efforts, a select set of particle diameters,  $D = [0.1, 0.3, 0.6, 1.0, 2.0, 3.0, 4.0, 5.0, 6.0, 7.0, 8.0, 9.0, 10.0]$ , was chosen for the trial solution vector set. The set  $D$  forms a partition of the IMD, as can be seen in Figure 19. For the MSE analysis, the trial IMD's were generated using a piecewise linear fit, as is illustrated in Figure 19.

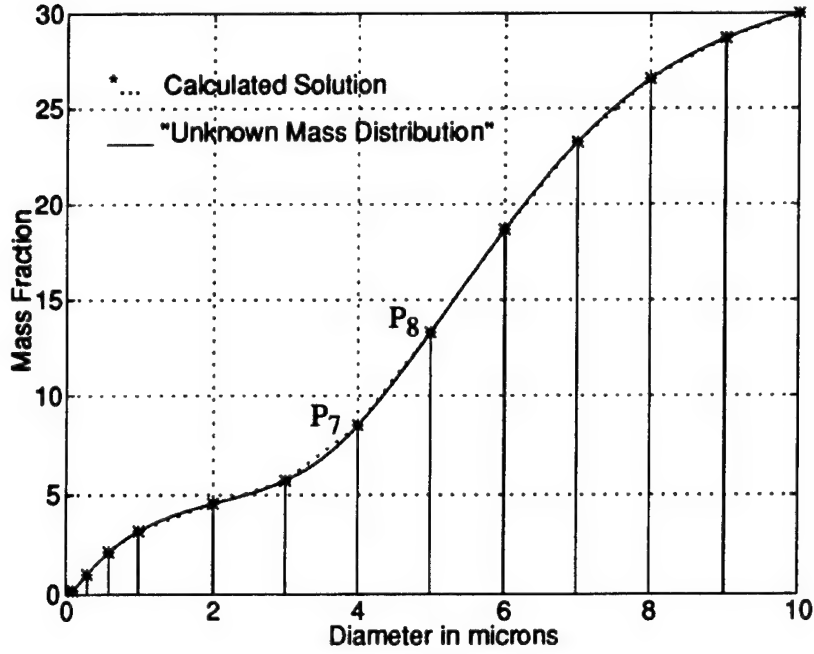


**Figure 19**  
**Integrated Mass Distribution with Piecewise Fit Overlaid**

From this fitted IMD, the mass fraction for the particle diameters that lie between the partitions are interpolated from the piecewise linear fit.

$$MF(D) = \frac{\rho \frac{\pi}{6} D^3 \int_0^D n(x) dx}{\int_0^\infty n(x) dx} \quad (111)$$

The test intensity is calculated as follows

$$I_s = (I_i / (k^2 r^2)) \bar{\chi}_{bi} \cdot MF(D). \quad (112)$$

This equation is equivalent to

$$I_i = \sum_j f_{ij} \left( \frac{MF(D_j)}{\rho \frac{\pi}{6} D_j^3} \right). \quad (113)$$

Using the IMD reduces the dimensionality of the solution space, which is actually a function space, by limiting the GA's search to monotonically increasing functions. Nonetheless, the salient features needed to find the PSDF were retained. The results were very encouraging, as the two



plots in Figure 20 show. The first plot shows the estimated IMD, the second shows the matched test intensity. The PSDF can be calculated from the IMD as follows

$$\text{PSDF} = n(D_j) = \frac{\text{MF}(D_j)}{\rho \frac{\pi}{6} D_j^3} \quad (114)$$

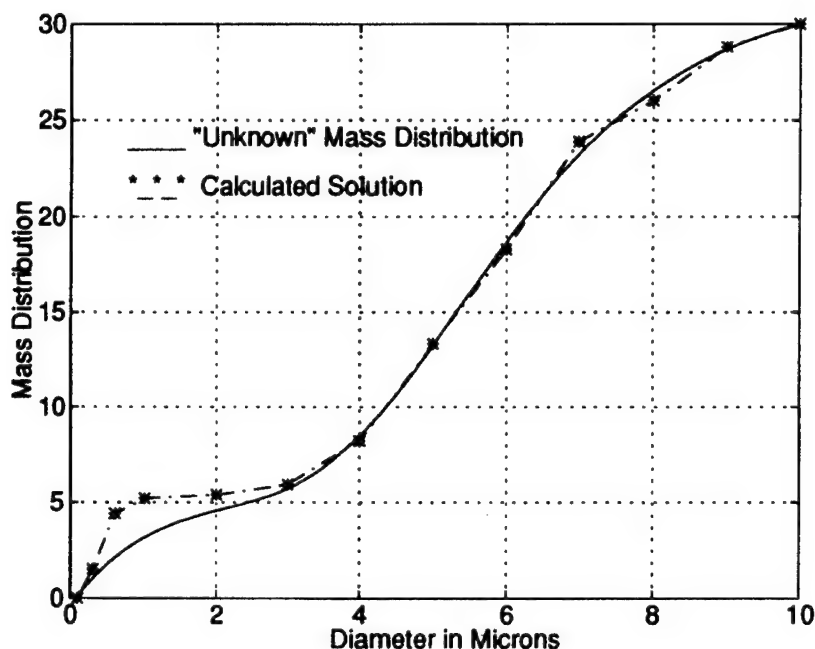


**Figure 20**  
**Preliminary Results Derived with SAGA**

As can be seen in all the estimated intensity plots presented so far, the scattered intensity is largely insensitive to variations in the PSDF for small particles.

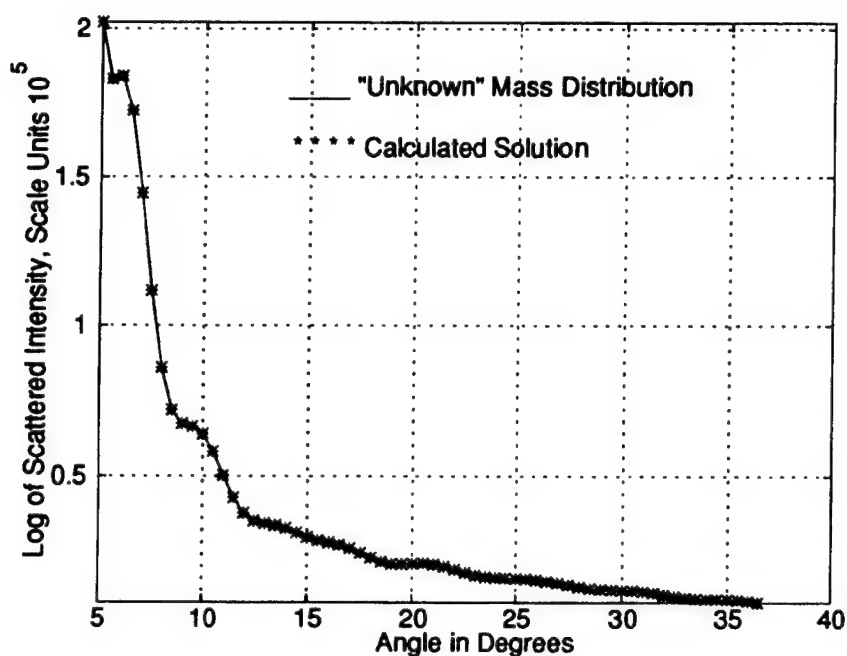


**Figure 21**  
**Comparison of SAGA Derived with Unknown Intensities**

In an effort to improve the resolving power of the GA for the small particle sizes, a modified mutation operator was added that would operate on particle sizes from  $0.1\mu\text{m}$  to  $4.0\mu\text{m}$  after every  $n$  iterations. This greatly improved the results, as shown in Figure 22.

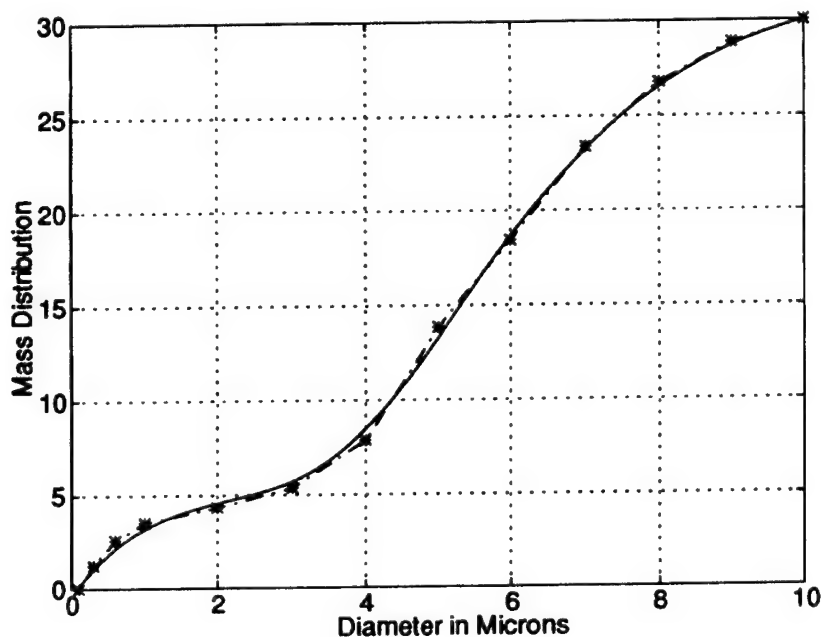


**Figure 22**  
**Improved Results After Modifications with SAGA**

To gain more insight into the performance of SAGA, a Gaussian monomodal distribution (GMD) with a narrow distribution width was created. As can be expected, the resolution that the GA can generate is dependent upon the partition width. Thus, adding more particle diameters to the select set of particle diameters,  $D$ , solves the problem. Figure 23 shows the before-and-after results. Improvement in the solution can be seen. The new particle diameters were added to the  $0.1\mu\text{m}$  to  $4.0\mu\text{m}$  range. The resolution of the GA's approximation would improve by the addition of partitions. However, from an instrumentation and computational perspective, it would be advantageous to keep a fixed number of partitions. Thus, the spacing of partitions must be made variable as a function of the trial solution fitness. This could be done by adding partition position information in the form of a vector segment to the vectors that make up the set of trial solutions. Further performance enhancements could be made by making the operator selection probability variable. Except for the AGA, all operator selection probabilities have been fixed. Even so, convergence to a solution has occurred in about 100 iterations.

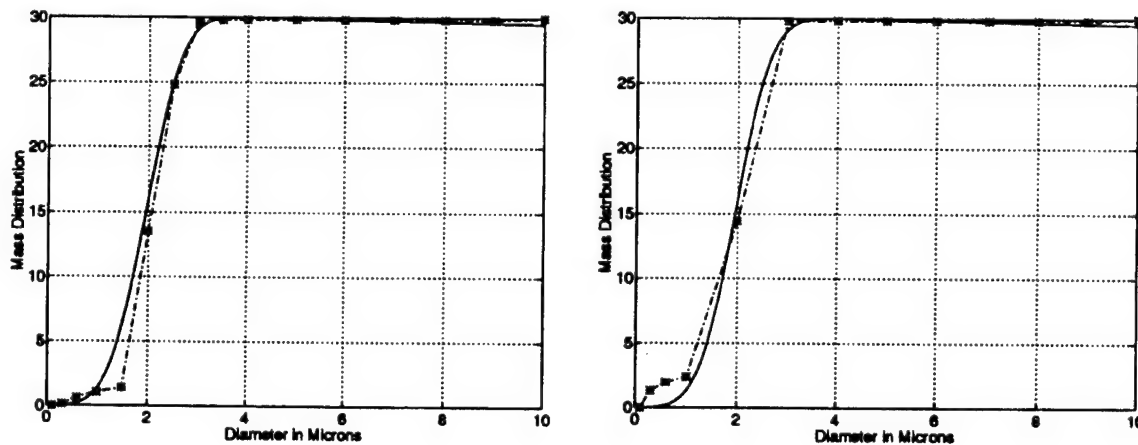


**Figure 23**  
**Before-and-After Results**

In conclusion, then, the GA offered the unique combination of stochastic search and exploration of promising solution space areas that was needed. The stochastic search was accomplished by perturbing randomly selected members of the solution set, while exploration was accomplished by retention of promising vector segments in the set of trial solutions. As the GA continued to process the trial solutions, an optimal solution was developed. The convergence rate was usually exponential. Accuracy of the solution could be improved by letting the GA decide which particle diameters are represented by the trial solutions. This could be accomplished by including in each trial solution a vector string that encoded the diameter values. The GA would process the diameters in the same manner that it does on the particle mass fractions.

## 8.0 CONCLUSIONS AND SUMMARY

The following conclusions were reached during the analysis and design of the *in-situ* probe.

- The complex index of refraction can be measured for an ensemble of particles using ellipsometric techniques.
- The ensemble average temperature can be determined by measuring the complex index of refraction and applying the Russian formula.
- Can not determine the effects that exhaust gases have on aluminum oxide particles from *in-situ* measurements alone.
- To improve measurement accuracy, the single scattering approximation must be maintained in the sampling volume at all times.
- Only off-axis forward measurements are needed to determine the optical properties and the particle size distribution.
- Traditional analytic inverse scattering methods will not provide accurate answers over the wide range particle sizes.
- The genetic algorithm, which is a subclass of the guided random search techniques, has proven capable of extracting the PDF for a wide range of particle diameters.
- The Integrated PDF is superior for use in the particle size distribution analysis.

The ellipsometric techniques borrowed from astronomy and solid state physics can be used to measure the optical properties of an aerosol, notably the imaginary index of refraction. Having made measurements of the complex index of refraction and the particle size distribution function, an empirical formula can be used to estimate the emissivity. We can verify the accuracy of the Russian model with our own by comparing the emissivities calculated by both models. However, without models of the physics of  $\text{Al}_2\text{O}_3$  at its melting point, the effects on the emissivity by the concentration and composition of exhaust plume gasses cannot be determined.

The typical analysis of particle size, shape, and optical properties requires measurements of the scattered intensity at many angles. By separating the optical properties measurements from the particle sizing measurements, only the forward angles, unlike the back scattering angles which are sensitive to variations in the imaginary part of the complex index of refraction, are needed. The particle concentration must be regulated in such a way that the single scattering model can be used to prevent the intensity as a function of angle signature of each particle from being smeared out.

The badly conditioned inversion matrix creates a situation whereby the use of analytic methods cannot produce unique solutions to the particle size distribution. Since the true solution is unknown, there is no guiding principle for the determination of the correct solution. By solving for the larger particles first, the GA has increased sensitivity to the presence of the smaller particles. In essence, the GA creates a guiding principle as it proceeds to the correct solution. Thus, it has superior performance over the analytic and other optimization methods. In addition, the GA can average out any noise present in the input signal. This is a by-product of the crossover operator making the resulting PDF solution robust in the presence of perturbations.

Further improvements in the GA can be made to improve convergence to the solution and increase the speed of calculation. These improvements would include: Compiling the code and implementing some sort of crossover adaptability based upon the convergence rate of the past several iterations

In summary, this report discussed the motivation behind the design and development of an *in-situ* optical probe. The report continued with the development of the theory needed to make the measurements of the optical properties and developed an estimate of the sampling time required to make the measurements statistically meaningful. Consideration was given to the effects that the optical properties play in the scattering of light by the particles; scanning angles and incident polarizations were chosen that would minimize these effects. Discussion then proceeded to the analysis of the PSDF, with recognition given to the degree of difficulty given in applying analytic methods. Various optimization methods were mentioned, with Genetic Algorithms standing out as exceptional. The GA motif was further developed with noted achievements as the conversion from the standard hill climber to minimizer. The report closed on the note that the PSDF was discernible by transforming it into the equivalent IMD and recommendations given as to further improvements in the GA approach.

## 9.0 REFERENCES

1. Nelson, H.F., "Influence of Scattering on Infrared Signatures of Rocket Plumes," *AIAA J. of Propulsion*, Jul 1983.
2. Dash, S.M., "Analysis of Exhaust Plumes and Their Interaction with Missile Airframes," Ed. M Summerfield, A87-22926 08-02, *Tactical Missile Aerodynamics*, American Institute of Aeronautical Astronautics, NY, Vol. 104, 1986, pp. 778-851.
3. Pluchino, A.B., Masturzo, D.E., "Emissivity of  $\text{Al}_2\text{O}_3$  Particles in a Rocket Plume," *AIAA Journal*, Vol. 19, No. 9, 1981, pp. 1234 - 1237.
4. Victor, A.C., "Effects of Multiple Scattering on Rocket Exhaust Plume Smoke Visibility," *J. Spacecraft and Rockets*, Vol. 26, No. 4, Jul-Aug. 1989, pp. 274-278.
5. Lyons, R.B., Wormhoudt, J., Gruninger, J., "Scattering of Radiation by Particles in Low Altitude Plumes," *AIAA 16th Thermophysics Conference*, Jun 23-25, Palo Alto, Ca.
6. Reed, R.A., Calia, V.S., "Review of Aluminum Oxide Rocket Exhaust Particles," *AIAA Paper 93-2819, AIAA 28th Thermophysics Conference, Orlando Fl, Jul 6-9, 1993.*
7. Rawlins, W.T., Green, B.D., "Spectral Signatures of Micron-sized Particles in the Shuttle Optical Environment," *Applied Optics*, Vol. 26, No. 15, Aug 1, 1987, pp. 3052-3060.
8. Hermesen, R.W., "Aluminum Oxide Particle Size for Solid Rocket Motor Performance Prediction," *J. Spacecraft*, Vol. 18, No. 6, Nov-Dec 1981, pp. 483-490.
9. Burkhard, D.G., Lochheas, J.V.S., Penchina, C.M., "On the Validity of Kirchhoff's Law in a Nonequilibrium Environment," *American Journal of Physics*, Vol. 40, Dec 1972, pp. 1794-1798.
10. Anfimov, N.A., Karabadjak, G.F., Khmelinin, B.A., Plastinin, Y.A., Rodionov, A.V., "Analysis of Mechanisms and Nature of Radiation from Aluminum Oxide in Different Phase States in Solid Rocket Exhaust Plumes," *AIAA Paper 93-2818, AIAA 28th Thermophysics Conference, Jul 6-9, 1993, Orlando Fl.*
11. Glazov, V.M., Chizhevskaya, S.N., Glagoleva, N. N., *Liquid Semiconductors*, Plenum Press, New York, 1969.
12. Kittel, C., *Introduction to Solid State Physics*, 3rd ed, "Chap 10, Semiconductor Crystals," John Wiley & Sons, Inc., New York, 1966, pp. 301-331.
13. Kittel, C., *Introduction to Solid State Physics*, 3rd ed, "Chap 18, Point Defects in Solids," John Wiley & Sons, Inc., New York, 1966, pp. 561-587.
14. Ziman, J. M., *Principles of the Theory of Solids*, 2nd ed., Cambridge University Press, Cambridge, MA, 1972.
15. Mott, Nevill, *Conduction in Non-Crystalline Materials*, Clarendon Press, Oxford, 1987.
16. Kettrup, T., "Urbach's Rule Derived from Thermal Fluctuations in the Band-gap Energy," *Physical Review, B*, Vol. 18, No. 6, Sep 15, 1978. pp. 2622-2631.
17. Weber, J.K.R., Anderson, C.D., Merkley, D.R., Nordine, P.D., "Solidification Behavior of Undercooled Liquid Aluminum Oxide," *J.Am.Ceram.Soc*, Vol. 78, No. 3, 1995, pp. 577-582.

18. Weber, J.K.R., Anderson, C.D., Krishnan, S., Nordine, P.D., "Spectral Absorption Coefficient of Molten Aluminum Oxide from 0.385 to 0.780  $\mu\text{m}$ ," *J. Am. Ceram. Soc.*, Vol. 78, No. 3, 1995, pp. 583-587
19. Brecher, C., Wei, G.C., Rhodes, W.H., "Point Defects in Optical Ceramics: High-Temperature Absorption Processes in Lanthana-Strengthened Yttria," *J. Am. Ceram. Soc.* Vol. 73, No. 6, Jun 1990, pp. 1473-1488.
20. Plass, G.N., "Temperature Dependence of the Mie Scattering and Absorption Cross Sections for Aluminum Oxide," *Applied Optics*, Vol. 4, No. 12, Dec 1965, pp. 1616-1619.
21. Innocenzi, M.E., Swimm, R.T., Bass, M., French, R.H., Villaverde, A.B., Kokta, M.R., "Room-temperature Optical Absorption in Undoped  $\alpha\text{-Al}_2\text{O}_3$ ," *J. Appl. Phys.* Vol. 67, No. 12, Jun 15, 1990, pp. 7542-7546
22. Lorrain, C., Corson, D., **Electromagnetic Fields and Waves**, W. H. Freeman and Co., San Francisco, CA, 1970.
23. Bohren, C., and Huffman, D., **Absorption and Scattering of Light by Small Particles**, John Wiley & Sons, Inc., New York, 1983.
24. Deirmendjian, D., **Electromagnetic Scattering on Spherical Polydispersions**, American Elsevier Publishing Company, Inc., New York, 1969.
25. Krishnana, S., "Calibrations, Properties, and Applications of the Division-of-Amplitude Photopolarimeter at 632.8 and 1523  $\mu\text{m}$ ," *J. Optical Society of America, A*, Vol. 9, No. 9, Sep 1992, pp. 1615-1622.
26. Thompson, R.C., Bottinger, J.R., Fry, E., "Measurement of Polarized Light Interactions via the Mueller Matrix," *Applied Optics*, Vol. 19, No. 8, Apr 15, 1980, pp. 1323-1332.
27. Hauge, P. S., "Recent Developments in Instrumentation in Ellipsometry," *Surface Science*, Vol. 96, 1980, pp 108-140.
28. Povel, H.P., Keller, C.U., Yadigaroglu, I.A., "Two-dimensional Polarimeter with Charge-coupled-device Image Sensor and a Piezoelectric Modulator," *Applied Optics*, Vol. 33, No. 19, Jul 1, 1994, pp. 4252-4260.
29. Ishimaru, Akira, **Wave Propagation and Scattering in Random Media, Vol. 1, Single Scattering and Transport Theory**, Academic Press, New York, 1978.
30. Ishimaru, Akira, **Wave Propagation and Scattering in Random Media, Vol. 2, Multiple Scattering, Turbulence, Rough Surfaces, and Remote-Sensing**, Academic Press, New York, 1978.
31. Stockham, J., Fochtman, E., **Particle Size Analysis**, Ann Arbor Science Publishers, Inc, Ann Arbor, MI, 1978.
32. Schuerman, D.W., Wang, R.T., Gustafson, B.A.S., and Schaefer, R.W., "Systematic Studies of Light Scattering. 1: Particle Shape," *Applied Optics*, Vol. 20, No. 23, Dec 1981, pp. 4039-4050.
33. Holland, A.C. and Gagne, G., "The Scattering of Polarized Light by Polydisperse Systems of Irregular Particles," *Applied Optics*, Vol. 9, No. 5, May 1970, pp. 1113-1121.

34. Bartholdi, M., Salzman, G.C., Hiebert, R.D., and Kerker, M., "Differential Light Scattering Photometer for Rapid Analysis of Single Particles in Flow," *Applied Optics*, Vol. 19, No. 10, May 15, 1980, pp. 1573-1581.
35. Traineau, J.C., Kuentzmann, P., et. al., "Particle Size Distribution Measurements in a Sub-scale Motor for the Ariane 5 Solid Rocket Booster," AIAA Paper 92-3049, AIAA/SAE/ASME/ASEE 28th Joint Propulsion Conference and Exhibit, Jul 6-8, 1992.
36. Salita, Mark, "Quench Bomb Investigation of  $\text{Al}_2\text{O}_3$  Formation from Solid Rocket Propellants (Part 2): Analysis of Data," NAS-30490, Morton Thiokol, Inc., Brigham City UT, pp. 185-197.
37. Asano, S., "Light Scattering Properties of Spherical Particles," *Applied Optics*, Vol. 18, No. 5, Mar 1, 1979, pp. 712-723.
38. Powell, E.A., Cassanova, R.A., Bankston, C.P., Zinn, B.T., "Combustion Generated Smoke Diagnostics by Means of Optical Measurement Techniques," *AIAA 14th Aerospace Sciences Meeting, Washington, D.C., Jan 26-28, 1976*
39. Kim, H.O., Laredo, D., Netzer, D.W., "Measurement of Submicrometer  $\text{Al}_2\text{O}_3$  Particles in Plumes," *Applied Optics*, Vol. 32, No. 33, Nov 20, 1993, pp. 6834-6840.
40. Klett, J.D., "Anomalous Diffraction Model for Inversion of Multispectral Extinction Data Including Absorption Effects," *Applied Optics*, Vol. 23, No. 24, Dec 15, 1984, pp. 4499-4508.
41. Hirleman, E.D., "Modeling of Multiple Scattering Effects in Fraunhofer Diffraction Particle Size Analysis," *Part. Part. Syst. Charact.*, Vol. 5, 1988, pp. 57-65.
42. Shah, H.S., Mehta, R.V., Desai, R.V., "Estimation of Particle Size Distribution Parameters with Forward-scattering Techniques," *Applied Optics*, Vol. 18, No. 24, Dec 15, 1979, pp. 4173-4177.
43. Dobbins, R.A., Crocco, L., Glassman, I., "Measurement of Mean Particle Sizes of Sprays from Diffractively Scattered Light," *AIAA Journal*, Vol.1, No. 8, Aug 1963, pp. 1892-1886.
44. Curry, B., "Constrained Eigenfunction Method for the Inversion of Remote Sensing Data -- Application to Particle Size Determination from Light Scattering Measurements," *Applied Optics*, Vol. 28, No. 7, Apr 1, 1989, pp. 1345-1355.
45. Strang, Gilbert, "The Fundamental Theorem of Linear Algebra," *The American Mathematics Monthly*, Vol. 100, No. 9, Nov 1993, pg 848-866.
46. Bulirsch, R. and Stoer, J., **Introduction to Numerical Analysis**, 2nd Ed., Springer-Verlag, New York, 1993.
47. Nievergelt, Yves, "Numerical Linear Algebra on the HP-28 or How to Lie with Supercalculators," *The American Mathematics Monthly*, Jun 1991, pp. 539-544.
48. Box, M.J., Davies, D., Swann, W.H., **Non-Linear Optimization Techniques**, Oliver & Boyd, Edinburgh, Scotland, 1969.
49. Press, W.H., Teukolsky, S.A., Vetterling, W.T., Flannery, B.P., **Numerical Recipes in Fortran**, 2nd ed., Cambridge University Press, Cambridge, MA, 1992.



50. Davis, L., ed, **Genetic Algorithms and Simulated Annealing**, Morgan Kaufmann Publishers, Inc., San Francisco, CA, 1987.
51. Nelder, J.A. and Mead, R., "A Simplex Method for Function Minimization," *The Computer Journal*, Vol. 7, 1965, pp. 308-313.
52. Fymat, A.L., Smith, C.B., "Analytical Inversions in Remote Sensing of Particle Size Distributions. 4: Comparison of Fymat and Box-Mckellar Solutions in the Anomalous Diffraction Approximation," *Applied Optics*, Vol.18, No. 21, Nov 1, 1979, pp. 3595-3598.
53. Dobbins, R.A., Strand, L.D., "A Comparison of Two Methods of Measuring Particle Size of  $\text{Al}_2\text{O}_3$  Produced by a Small Rocket Motor," *Technical Report 32-1383*, JPL, Jun 1, 1969.
54. Hansom, R. J., "A Numerical Method for Solving Fredholm Integral Equations of the First Kind using Singular Values," *SIAM J. Numer. Anal.*, Vol. 8, No. 3, Sep 1971. pp. 616-622.
55. Razzaghi, M., Razzaghi, M., Arabshahi, A., "Solutions of Convolution Integral and Fredholm Integral Equations via Double Fourier Series," *Applied Mathematics and Computation*, Vol. 40, 1990, pp. 215-224.
56. Azzopardi, B.J., "Measurement of Drop Sizes," *Int. J. Heat Mass Transfer*, Vol. 22, 1979, pp. 1245-1279.
57. Baker, C.T.H., Fox, L., Mayer, D.F., Wright, K., "Numerical Solution of Fredholm Integral Equations of First Kind," *J. Comput.*, Vol. 7, 1964, pp. 141-148.
58. Phillips, D. L., "A Technique for the Numerical Solution of Certain Integral Equations of the First Kind," *J. Assoc. Comput. Mach.*, Vol. 9, 1962, pp. 84 - 97.
59. Landweber, L., "An Iteration Formula for Fredholm Integral Equations of the First Kind," *Am. J. Math.*, Vol. 73, 1951, pp. 615-624.
60. Shifrin, K.S., Truchin, V.F., Turovtseva, L.S., Gashko, V.A., "Reconstruction of Particle Size Distribution by Statistical Regularization of the Scattering Function," *Atmospheric and Oceanic Physics*, Vol. 8, No. 12, 1972, pp. 739-743.
61. Holve, D, Self, S.A., "Optical Particle Sizing for In Situ Measurements, Part 1," *Applied Optics*, Vol. 18, No. 10, May 15, 1979, pp. 1632-1645.
62. Westwater, E.R., Cohen, A., "Application of Backus-Gilbert Inversion Technique to Determination of Aerosol size Distributions form Optical Scattering Measurements," *Applied Optics*, Vol. 12, No. 6, Jun 1973, pp. 1340-1438.
63. Shaw, G., "Inversion of Optical Scattering and Spectral Extinction Measurements to Recover Aerosol Size Spectra," *Applied Optics*, Vol. 18, No. 7, Apr 1979, pp. 988-993.
64. Twomey, S., "Information Content in Remote Sensing," *Applied Optics*, Vol. 13, No. 4, Apr 1974, pp. 942-945.
65. Capps, C.D., Henning, R.L., and Hess, G.M., "Analytic Inversion of Remote-Sensing Data," *Applied Optics*, Vol. 21, No. 19, Oct 1, 1982, pp. 3581-3587.
66. Dellango, C. and Horvath, H., "On the Accuracy of the Size Distribution Information Obtained from Light Extinction and Scattering Measurements. 1. Basic Considerations and Models," *J. Aerosol Sci.*, Vol. 24, No. 2, 1993, pp. 129-141.

67. Smithies, F., **Integral Equations**, Cambridge University Press, Cambridge, MA, 1958.
68. Goldberg, David, **Genetic Algorithms in Search, Optimization & Machine Learning**, Addison-Wesley Publishing Company, Inc., Reading, MA, 1989.
69. Michalewicz, Zbigniew, **Genetic Algorithms + Data Structures = Evolution Programs**, Springer-Verlag, New York, 1992.
70. Davis, Lawrence, "Adapting Operator Probabilities In Genetic Algorithms," *Proceedings of the Third International Conference on Genetic Algorithms*, Morgan Kaufman Publishers, San Francisco, CA, 1989, pp 61- 69.
71. Davis, Lawrence, **Handbook of Genetic Algorithms**, Van Nostrand Reinhold, New York, 1991.
72. Baker, J.E., "Reducing Bias and Inefficiency in the Selection Algorithm," *Proceedings of the Second International Conference on Genetic Algorithms*, Lawrence Erlbaum Associates, Hillsdale, NJ, 1987, pp 14 - 21.
73. Kennedy, Scott, A., "Five Ways to a Smarter Genetic Algorithm," *AI Expert*, Dec 1993, p. 35-38.